

1 **Dysregulation of neuroproteasomes by ApoE isoforms drives endogenous Tau aggregation**

2
3 Paradise V^{1,2}, Sabu M^{1,2}, Bafia J³, Sharif NA^{1,2}, Nguyen C^{1,2}, Konrad-Vicario KD^{1,2}, Dhanraj
4 Mukim R^{1,2}, Wang X^{1,2}, Corjuc BT^{1,2}, Fu J⁴, Maldonado G^{1,2}, Ndubisi J^{1,2}, Strickland M⁵,
5 Figueroa H¹, Almeida D^{1,2}, Hyman B⁶, Holtzman DM⁵, Nuriel T¹, Ramachandran KV^{1,2,7*}

6
7 1 Taub Institute for Research on Alzheimer's Disease and the Aging Brain, Columbia University
8 Vagelos College of Physicians and Surgeons, New York, NY 10032

9 Taub Institute for Research on Alzheimers Disease and the Aging Brain, Columbia University
10 Vagelos College of Physicians and Surgeons, New York, NY 10032

11 2 Department of Neurology, Columbia University Irving Medical Center. New York, NY 10032

12 3 Department of Molecular and Cellular Biology, Harvard University, Cambridge, MA 02139

13 4 Program in Medical and Population Genetics, Broad Institute of MIT and Harvard, Cambridge,
14 MA

15 5 Department of Neurology, Hope Center for Neurological Disorders, Knight Alzheimers
16 Disease Research Center, Washington University School of Medicine, St. Louis, MO 63110

17 6 Alzheimer Research Unit of the MassGeneral Institute for Neurodegenerative Disease,
18 Department of Neurology of the Massachusetts General Hospital, and Harvard Medical School,
19 Charlestown, Massachusetts 02129-4404

20 7 Department of Neuroscience, Columbia University Vagelos College of Physicians and
21 Surgeons, New York, NY 10032

22 *To whom correspondence should be addressed: kvr2113@cumc.columbia.edu

23
24 Neuroproteasomes are a subset of 20S proteasomes that are localized to the neuronal plasma
25 membrane and degrade newly synthesized proteins. To date, the molecular composition of
26 neuroproteasomes is undefined, and moreover, whether neuroproteasomes can influence protein
27 aggregation with relevance to neurodegenerative disorders remains unexplored. Using a Cre-
28 dependent conditional knock-in mouse line to endogenously tag the proteasome, we find that
29 neuroproteasomes co-purify with ApoE, the most significant risk factor for late-onset
30 Alzheimer's Disease (AD). We discover that neuroproteasome membrane localization is
31 differentially modulated by ApoE isoforms (E4<E3<E2) *in vitro*, *in vivo*, and in human
32 postmortem samples. We synthesized selective, neuroproteasome-specific inhibitors and
33 discovered that neuroproteasome inhibition induces aggregation of endogenous mouse and
34 human Tau, without the need for seeding or pathogenic mutations. Using hApoE-KI/hTau-KI
35 crosses, we find that ApoE isoforms differentially shift the aggregation threshold for Tau.
36 Neuroproteasome inhibition *in vivo* is sufficient to induce sarkosyl-insoluble and Thioflavin-S
37 positive endogenous Tau aggregates in only three days, which are completely abrogated by co-
38 application of cycloheximide. Newly synthesized Tau levels increase threefold after
39 neuroproteasome inhibition, leading us to posit that newly synthesized Tau is uniquely
40 susceptible to aggregation due to neuroproteasome dysfunction. Overall, our data define
41 neuroproteasomes as a pivotal proteostasis mechanism underlying the formation of endogenous
42 Tau aggregates, which is directly regulated by the largest genetic risk factor for late-onset
43 Alzheimer's Disease.

44 **Introduction**

45
46 Protein homeostasis mechanisms define the cellular capacity to handle protein synthesis, folding,
47 and clearance while minimizing the accumulation of deleterious protein misfolding and
48 aggregation events. While many factors contribute to protein homeostasis, protein degradation
49 serves as a critical and non-redundant determinant of cellular proteostatic capacity. In canonical
50 models of protein degradation, proteins are either degraded by the ubiquitin-proteasome system
51 or the endo-lysosomal and autophagic systems(1, 2). In contrast to the established paradigms of
52 protein degradation, we recently described the neuroproteasome, which is localized to the
53 neuronal plasma membrane, exposed to the extracellular space, and degrades intracellular
54 substrates across the membrane(3). We interpret this to mean that the neuroproteasome is
55 functionally transmembrane(3). In addition, neuroproteasomes are composed of the 20S core
56 proteasome and lack the canonical 19S cap and therefore, cannot recognize ubiquitylated
57 substrates or unfold them for degradation. Instead, neuroproteasomes co- or peri-translationally
58 degrade newly synthesized proteins without the need for ubiquitylation(4). While multiple
59 reports have demonstrated the existence of neuroproteasomes in diverse systems(5), the
60 molecular composition of neuroproteasomes, the regulation underlying neuroproteasome
61 membrane localization, and the function of neuroproteasomes *in vivo* are poorly defined.
62

63 Failures in protein homeostasis are linked to accumulation of protein inclusions and aggregates.
64 Indeed, Alzheimer's Disease (AD) and many other neurodegenerative diseases are linked by the
65 accumulation of protein aggregates(6, 7). Tau aggregates are among the most common
66 intracellular aggregates in AD and are characteristic of more than 20 neurodegenerative diseases,
67 termed Tauopathies(8). Multiple mutations that render Tau more prone to aggregation have been
68 identified in patients(9) and these have been extensively modeled in transgenic lines and iPSC-
69 derived neurons(10-13). While these studies have provided important insights into the
70 mechanisms of Tau aggregate clearance, genetic variants in *MAPT* only make up less than 5% of
71 the total population with AD and Tauopathies(14-18). Instead, endogenous Tau aggregates are
72 found in the absence of overexpression or mutations in *MAPT* in the majority of patients with
73 sporadic AD(19, 20). The protein quality control mechanisms in neurons that prevent
74 endogenous Tau from aggregating remain elusive.
75

76 Moreover, aggregated Tau can induce the further aggregation of otherwise normal Tau, creating
77 a feed-forward prion-like propagation referred to as Tau seeding(12, 21, 22). Studies delineating
78 the principles of Tau seeding and propagation have provided new insights into the development
79 of Tau pathology. Yet, the mechanisms underlying the initial aggregate formation in this
80 pathological context are unclear. Therefore, identifying mechanisms by which endogenous Tau
81 aggregates form could provide a unique therapeutic opportunity for intervention before Tau
82 seeds can promote further templating and propagation.
83

84 While failures of the endolysosomal and autophagic systems can exacerbate Tau aggregation(23-
85 26), whether and how proteasomal dysfunction affects Tau aggregation is contested. Multiple
86 reports demonstrate that proteasomes can degrade Tau *in vitro* and in heterologous cells (27-30).
87 However, follow up studies demonstrated that proteasome inhibition in neurons neither increases
88 Tau levels nor does it induce endogenous Tau aggregation(31-34). In fact, somewhat
89 counterintuitively, proteasomal inhibition leads to the reduction of soluble Tau due to the
90 compensatory induction of autophagy in neurons(31-34). However, proteasomes can be involved
91 in clearing already aggregated Tau but require the help of ATPases such as VCP to unfold the
92 aggregates(35). The mechanisms by which protein degradation machineries determine both the
93 formation and clearance of endogenous Tau aggregates are still debated. The discovery of the
94 neuroproteasome provides a new mechanism to interrogate how protein degradation could
95 contribute to the formation and clearance of protein aggregates in neurons.
96

97 While the precise mechanisms underlying Tau aggregation remain a subject of intense
98 investigation, one major genetic factor that influences Tau aggregation and many other
99 phenotypes in neurodegeneration is ApoE(36-38). The most significant risk factor for sporadic
100 Alzheimer's Disease is the ApoE4 isoform of the ApoE gene, while the ApoE3 isoform is neutral
101 and the ApoE2 isoform is protective(39, 40). The mechanisms by which ApoE isoforms confer
102 dramatic differences in the risk for AD remains unclear, but it is well established that ApoE4 is
103 associated with increased Amyloid β and Tau pathology(37, 41, 42). More specifically, it
104 remains mechanistically vague how ApoE isoforms influence Tau aggregation and
105 neurodegeneration. Gaining the biochemical and cell biological insights connecting ApoE
106 isoforms and Tau turnover could be invaluable to revealing the mechanisms underlying
107 neurodegeneration.
108

109 Here, we discover an unexpected link between ApoE and endogenous Tau aggregation through
110 the neuroproteasome. Using a transgenic mouse line to endogenously and conditionally tag the
111 20S proteasome coupled with quantitative proteomics, we found that neuroproteasomes co-
112 purify with ApoE. Neuroproteasome localization at the plasma membrane is differentially
113 regulated by ApoE isoforms, with ApoE4 reducing localization and ApoE2 increasing
114 localization relative to ApoE3, *in vivo*, in primary neurons, and in humans. Using an unbiased
115 quantitative proteomic screen, we identify neuronal responses to neuroproteasome inhibition in
116 the soluble and insoluble proteome. Neuroproteasome dysfunction leads to deficits in
117 proteostasis and induces aggregation of endogenous Tau in primary neurons and *in vivo*. We find
118 that ApoE4 reduces the threshold at which Tau aggregates by ~ 25-fold compared to ApoE3 and
119 ~200-fold compared to ApoE2, thereby dramatically elevating risk for Tau aggregation due to
120 neuroproteasome dysfunction. Neuroproteasome-inhibition-induced endogenous Tau inclusions
121 migrate as a high molecular weight species, which is typically reported only in the AD brain or
122 with seeding-competent Tau(43-46). Using quantitative phosphoproteomic analysis supported by
123 imaging in primary neurons and *in vivo*, we find that neuroproteasome inhibition induces the

124 phosphorylation of Tau at sites consistent with pathological aggregated Tau in the AD brain. We
125 suggest that neuroproteasomes serve as a pivotal proteostasis factor, mechanistically distinct
126 from canonical degradation systems, directly linking ApoE to the formation of endogenous Tau
127 aggregates.

128

129 Results

130

131 **Endogenous affinity tags on the 20S proteasome reveal that neuroproteasomes co-purify** 132 **with ApoE and Lrp1**

133

134 We sought to purify the neuroproteasome directly out of the mouse brain. Our attempts to do this
135 out of wild-type (WT) tissue proved challenging due to lengthy preparations which caused low
136 yields. To circumvent this, we built a transgenic mouse line to endogenously tag the 20S
137 proteasome for affinity purification. The proteasome is comprised of the 20S catalytic core
138 particle which, as part of the ubiquitin-dependent degradation system, can be terminally
139 associated with either one or two 19S regulatory particles, referred to as the 26S (20S+19S) or
140 30S (20S + two 19S) proteasome respectively. The 20S core is characterized by four axially
141 stacked heptameric rings: the outer alpha subunit rings which gate substrate entry and the inner
142 rings which contain the catalytic beta subunits. The 19S caps contain subunits to bind
143 ubiquitylated substrates and ATPases to unfold said substrates into the 20S core. Therefore,
144 modifying the 20S with affinity tags allows us to isolate any complex containing the core
145 proteasome, such as free 20S, singly-capped 26S, doubly-capped 30S proteasomes, or the
146 neuroproteasome. We modified the C-termini of nearly every core proteasome subunit with
147 either 6X-His or Strep-II tags and screened out constructs based on low expression and
148 interference with proteasome function (**Fig S1A**). Of the remaining two constructs, we found that
149 only the C-terminal modification of *Psma3* was compatible with proper proteasome assembly
150 and function and did not adversely affect cell health (**Fig S1B**). Based on these data, we
151 generated a 20S-FLAG transgenic line by adding flanking loxP sites surrounding the final exon
152 (Exon 11) of the *Psma3* gene followed by the same sequence with a linker containing a 3X-
153 FLAG tag (**Fig 1A**). By crossing 20S-FLAG transgenic mice with a line expressing Cre
154 recombinase driven by the pan-neuronal Actlb6 (BAF53b) promoter(47), we generated mice that
155 expressed FLAG-tagged proteasomes selectively in neurons (**Fig 1B**). Brains from 20S-
156 FLAG/BAF53b-Cre mice and Cre-only littermate controls were processed and FLAG-tagged
157 cytosolic proteasomes were isolated on beads with a nanobody against the FLAG epitope.
158 Simultaneously, 26S proteasomes were isolated using the GST-UBL affinity isolation
159 method(48) and all samples were immunoblotted using antibodies raised against multiple 19S
160 and 20S subunits. We find that the FLAG tag is incorporated into the proteasome and we fail to
161 detect any FLAG in the Cre-only littermate controls (**Fig 1B**).

162

163 We next measured the catalytic activity of the FLAG-tagged proteasome compared to
164 unmodified proteasomes by monitoring the cleavage of a model substrate, Suc-LLVY-AMC(49).
165 An increase in fluorescence reflects the proteasome-dependent cleavage of this LLVY substrate
166 which mobilizes the free fluorescence of AMC. We find that the catalytic activity of isolated 26S
167 proteasomes from mice expressing 20S-FLAG are indistinguishable from the unmodified
168 proteasomes isolated from controls (**Fig 1C**). We find that FLAG affinity purified proteasomes
169 are catalytically identical to 26S affinity purified proteasomes (**Fig 1C**). We fail to detect FLAG
170 expression in the livers from 20S-FLAG/Baf53b-Cre mice, nor can we affinity isolate
171 proteasomes using the FLAG epitope handle from the liver, indicative of the selective and
172 inducible nature of the 20S-FLAG transgene (**Fig S1C, D**). Overall, we find that mice expressing
173 20S-FLAG appear indistinguishable from wild-type littermates. These extensive
174 characterizations support the conclusion that epitope tagging of the 20S with FLAG is inert and
175 does not disrupt native proteasome function.
176

177 To test whether the 20S-FLAG was efficiently incorporated into the neuroproteasome, we
178 performed surface biotinylation experiments out of both primary neurons and hippocampal tissue
179 from 20S-FLAG transgenic mice. This is a well-established method for measuring
180 neuroproteasome surface localization(3, 50, 51). Hippocampi from 20S-FLAG/Baf53b-Cre mice
181 were incubated with a cell-impermeable sulfonylated Biotin-NHS-Ester to label surface-exposed
182 amines and surface proteins were pulled down on streptavidin beads. We observe strong FLAG
183 expression in the surface fraction, indicating that the FLAG tag is incorporated into the
184 neuroproteasome (**Fig 1D**). We fail to detect cytosolic proteins such as Actin in our surface
185 fraction, validating our surface-labeling approach, and fail to observe FLAG expression in 20S-
186 FLAG mice without Cre (**Fig 1D**). By blotting using an antibody which detects six of the seven
187 alpha subunits of the 20S proteasome including α_7 , the subunit coded for by *Psma3*, we can
188 clearly distinguish the modified α_7 subunit overlaying with the FLAG signal, denoting
189 modification of the endogenous protein (**Fig 1D**). Next, we used surface biotinylation to assess if
190 our transgenic system was functional in primary cultures. Primary neurons from 20S-FLAG mice
191 were cultured and transduced with AAVs to express Cre recombinase at days *in vitro* (DIV) two
192 and then processed for surface biotinylation at DIV14 (**Fig S1E**). We did not detect FLAG
193 without AAVs to express Cre, supporting our conclusion that the 20S-FLAG transgene is
194 inducible and not leaky.
195

196 Next, we purified FLAG-neuroproteasomes to determine their composition. First, we prepared
197 plasma membranes from 20S-FLAG/Baf53b-Cre brains and then gently extracted membrane
198 proteins. We find our membrane preparations were enriched in membrane proteins such as
199 GluR1 and depleted of cytosolic proteins like Actin (**Fig S1F**). We affinity isolated FLAG-
200 neuroproteasomes from the membrane fraction as well as cytosolic FLAG-proteasomes and
201 subjected both to quantitative tandem mass tag-based mass spectrometry analysis. As expected,
202 we find common signatures of 20S subunits between both cytosolic proteasomes and

203 neuroproteasomes and a significant depletion of 19S subunits in the neuroproteasome isolations.
204 This is consistent with a lack of cytosolic subunits in our membrane preparations and validates
205 our previous findings(3-5). We identified 64 proteins enriched in the neuroproteasome isolations
206 which are depleted in the cytosolic fraction. This revealed significant enrichment of the GPM6
207 glycoprotein, which we previously described(3) (**Fig 1E**), and a surprising and strong enrichment
208 of ApoE and the ApoE receptor Lrp1 (**Fig 1E, Table S1**). We do not observe other ApoE
209 receptors, such as ApoER2, VLDLR, and LDLR in this analysis. We first validated these
210 proteomic data by affinity isolating FLAG-neuroproteasomes as well as cytosolic FLAG-
211 proteasomes and then immunoblotting these samples. Here, we validate our proteomic data by
212 also identifying robust co-purification of ApoE and Lrp1 with the FLAG-neuroproteasome (**Fig**
213 **1F**).

214

215 **ApoE isoforms differentially modulate neuroproteasome surface localization *in vivo***

216

217 ApoE can be expressed as one of three isoforms in human: ApoE4, ApoE3, and ApoE2, each of
218 which differs by only one or two residues. We next tested whether ApoE isoforms could
219 differentially modulate neuroproteasome localization and function. We obtained human ApoE
220 isoform knock-in (KI) mice, where the entire coding region for the *Apoe* gene was replaced with
221 a cassette encoding the three human *Apoe* loci, generating a fully humanized ApoE protein(52).
222 These mice therefore only express the ApoE2, ApoE3, or ApoE4 isoforms. hApoE-KI mice were
223 perfused and then hippocampus and primary motor cortex (PMC) were microdissected and
224 subjected to surface biotinylation and immunoblotting. We chose a limited survey of regions
225 based on their differential susceptibility to accumulate pathological hallmarks of AD
226 (hippocampus>PMC)(53, 54). We found a strong reduction of neuroproteasome surface
227 localization in the hippocampus of ApoE4-KI mice, compared to ApoE3-KIs or ApoE2-KIs,
228 measured by surface signal of 20S subunit β 5 (**Fig 2A**). We observe a significant difference
229 between ApoE3 male and female mice, where female ApoE3 mice have 50% fewer surface-
230 localized neuroproteasomes than male ApoE3 mice in hippocampus (**Fig 2A**). We find this
231 noteworthy in the context of the extensive literature on the influence of biological sex on AD
232 pathogenesis(36, 55-58). When we monitor neuroproteasome localization in the PMC from the
233 hApoE-KI mice, we find that neuroproteasome surface localization in ApoE4-KIs is reduced
234 compared to ApoE2-KIs and we observe a trend, but no significant change in ApoE4-KI
235 compared to ApoE3-KI (**Fig S2A**). These data may be attributable to differences in ApoE
236 expression in different brain regions(36, 52, 59), a dimension which we have not systematically
237 investigated.

238

239 Given the region-specific effect of ApoE isoforms on neuroproteasome expression *in vivo*, we
240 approached the effect of ApoE isoforms and ApoE receptors in a more defined and tractable
241 primary neuronal culture system. Lrp1 was the only ApoE receptor that we identified in our
242 neuroproteasome IP/MS dataset and we also found ApoE isoform-dependent modulation of Lrp1

243 levels (**Fig S2B**). Instead of testing the role for Lrp1 specifically, we tested the role for ApoE
244 receptors in modulating neuroproteasome localization using the well-established pan-ApoE
245 receptor antagonist Receptor-associated protein (RAP) (60-62). We chose this strategy because
246 Lrp1 knockouts still contain small amounts of Lrp1 remaining in sporadic sets of neurons and
247 because of detrimental effects on neuronal health following Lrp1 knockdown(63, 64). We used a
248 variant of RAP (stable RAP) which contains a stabilizing mutation to protect against pH-induced
249 denaturation and maintains a higher percentage of internalized Lrp1, and presumably other ApoE
250 receptors as well(60) (**Fig 2B**). We incubated primary neurons with purified stable RAP and
251 measured surface protein levels using surface biotinylation and immunoblotting. We find that
252 stable RAP rapidly decreases the surface localization of Lrp1, as expected (**Fig 2C**). We also
253 find that stable RAP reduces surface localization of neuroproteasomes (**Fig 2C**). These data
254 served as the first demonstration that ApoE receptors, such as Lrp1, can regulate
255 neuroproteasome localization.
256

257 ApoE is a lipoprotein, and in the brain is thought to be released by glia in the lipid-bound
258 form(36, 52, 65, 66). We therefore next leveraged the primary culture system to determine
259 whether extracellular ApoE could modulate neuroproteasome localization and if the lipidation of
260 ApoE was important for this modulation. We generated primary neurons from either 20S-FLAG
261 transgenic animals or WT animals and conducted imaging and biochemical experiments to
262 measure neuroproteasome localization. We conjugated recombinant ApoE isoforms with a
263 mixture of POPC and Cholesterol (PC) and purified ApoE lipoproteins, referred to as PC-
264 ApoE2, E3, and E4. These lipoproteins were validated by SEC and negative stain EM (**Fig S2C**)
265 and have been demonstrated to resemble the endogenous ApoE lipoproteins observed in the
266 brain(67). DIV13 primary neurons from 20S-FLAG transgenic mice were incubated with
267 unconjugated or PC-conjugated ApoE for 24 hours and then subjected to surface biotinylation.
268 We find that PC-ApoE, and not the unconjugated versions, modify neuroproteasome surface
269 localization with the rank order PC-ApoE4<Vehicle,PC-ApoE3<PC-ApoE2 (**Fig 2D**). We find
270 no change in other membrane proteins such as GluN1, which has previously been shown not to
271 change in an ApoE isoform-dependent manner(68, 69). The lipoprotein-dependent effect on
272 neuroproteasome localization requires ApoE, as the addition of just the liposomes without ApoE
273 does not modify neuroproteasome localization (**Fig 2D**). We find similar results in primary WT
274 neurons, suggesting that the observed ApoE-isoform dependent effect on localization is not an
275 artifact of the FLAG epitope tag on neuroproteasomes (**Fig S2D**).
276

277 FLAG-neuroproteasomes are a useful tool to measure the surface localization of
278 neuroproteasomes and we next took advantage of the epitope tag to test whether ApoE isoforms
279 modified the subcellular distribution and localization of neuroproteasomes in intact neurons. We
280 used antibody feeding onto live neuronal cultures from the 20S-FLAG mice transduced with
281 AAVs to express Cre(70, 71). No staining was observed using secondary alone controls (**Fig**
282 **S2E**) or when feeding an antibody against intracellular protein MAP2 (**Fig S2F**). After live cell

283 anti-FLAG antibody feeding, neurons were fixed, permeabilized, and stained for total
284 intracellular MAP2 to label dendrites. Consistent with this approach being a robust measure of
285 neuroproteasome localization (**Fig S2G**), we observed punctal neuroproteasome localization
286 when feeding anti-FLAG antibodies, of which more than 90% was within 2 µm of the MAP2
287 signal. We observe significant overlap of surface FLAG signal with MAP2-positive protrusions
288 that resemble dendritic spines (**Fig 2E**). We observe that PC-ApoE2 increases neuroproteasome
289 surface localization by nearly twofold and that PC-ApoE4 reduces neuroproteasome surface
290 localization by nearly threefold compared to PC vehicle or PC-ApoE3 controls (**Fig 2E**). In total,
291 these data recapitulate the observations from the hApoE-KI mice and support our hypothesis that
292 extracellular ApoE isoforms can influence neuroproteasome localization and function.
293

294 **Neuroproteasome localization is reduced in vulnerable brain regions in the human brain
295 and is further reduced by ApoE4 genotype**

296
297 We next tested whether ApoE-dependent mislocalization of neuroproteasomes is observable in
298 postmortem patient tissues. For these analyses, we studied a cohort of 19 individuals (14
299 ApoE3/3 and 5 ApoE4/4) from the Massachusetts General Hospital Brain Bank. The ApoE3/3
300 subgroup was subdivided into 5 negative diagnoses and 9 positive diagnoses for AD. Sex was
301 evenly distributed in samples except for the ApoE4 cases which were all male. This design
302 allows us to compare the effect of AD on neuroproteasome localization as well as the effect of
303 ApoE genotype on neuroproteasome localization. We obtained material from the Brodmann Area
304 (BA4 – primary motor area) and BA7 (parietal associative area). We analyzed these regions as a
305 means of untangling how neuroproteasome localization changes in a limited survey of severely
306 pathologically affected (BA7) versus less affected (BA4) regions of the brain. Tissue from BA7
307 contained severe tangle and amyloid pathology as well as neuronal loss whereas tissue from BA4
308 had moderate amyloid pathology but not tangle accumulation or neuronal loss. For simplicity,
309 we will refer to BA7 as tissue with severe pathology and BA4 as tissue with mild pathology. We
310 fractionated these samples to remove nuclei, mitochondria, and cytosol, enriching for plasma
311 membranes and detergent-insoluble proteins. We monitored the success of our fractionation
312 using LLVY-based proteasome activity assays out of the supernatant of our washes and
313 continued washing our plasma membrane preparations until cytosolic proteasomes were
314 undetectable (**Fig 3A**).
315

316 We then subjected plasma membrane/aggregate fractions to quantitative TMT proteomics
317 analysis. TMT proteomics enables unbiased quantification of the proteome and the ability to
318 make quantitative comparison across samples. We compensated for brain region and individual
319 variability in two ways: by first normalizing protein loading into the mass spectrometer and then
320 normalizing the collected data against the total TMT signal per patient sample. This total TMT
321 signal normalization provides the highest confidence metric for protein abundance normalization
322 across all samples. Given the number of samples, we combined three TMTpro 16-plex

323 experiments with a shared internal standard which enabled quantitation across TMT experiments.
324 We first performed a series of quality control checks to ensure that these data provided reliable
325 and reproducible measures. First, these data validate our plasma membrane enrichment protocol
326 – we find a significant enrichment for membrane-bound and membrane-associated proteins and a
327 strong depletion of cytosolic proteins, including the 19S cap (**Table S2**). Second, consistent with
328 previous global proteomic analysis from AD brains, we find a significant increase of C4b(72),
329 AnxA1(73), Gpnmb(74), and Tau (Mapt)(75) in AD brains compared to unaffected controls (**Fig**
330 **3B**). Third, we also find a significant decrease in Vgf(76) and Slc30A3(77) consistent with
331 previous AD global proteomic datasets (**Fig 3B**). We expect to find aggregated proteins using
332 this protocol since our plasma membrane enrichment method would also isolate large aggregates
333 such as aggregated Tau in the AD brain.

334
335 After validating our approach, we next analyzed the effect of AD on neuroproteasome
336 localization, measured by the relative quantity of 20S proteasome subunits in our quantitative
337 mass spectrometry dataset. First, in comparing AD samples to cognitively normal controls, we
338 find a striking reduction in nearly every 20S proteasome subunit in the plasma membrane
339 fraction from BA7 tissue (**Fig 3B, Table S2**). We next sought to determine whether ApoE
340 genotype influenced neuroproteasome localization in human tissue. Given the significant effect
341 of AD on neuroproteasome localization, we constrained the analysis only to the effect of ApoE
342 genotype on neuroproteasome localization by comparing the ApoE4/4 AD cohort against the
343 ApoE3/3 AD cohort. We observe a clear trend of reduced 20S proteasome subunits in the
344 membrane fraction in the ApoE4 genotype compared to ApoE3 genotype in the BA7 vulnerable
345 brain region (**Fig 3C, Table S2**).
346

347 To validate our proteomics data, we monitored surface localization of neuroproteasomes by
348 immunoblot analysis. We controlled for sample loading by normalizing against Kv1.2, a protein
349 whose expression has been reproducibly demonstrated as unchanged in the AD brain(78-80).
350 While this strategy is required for loading controls by immunoblot, these loading controls line up
351 with the normalization strategy for mass spectrometry based on the total amount of TMT signal
352 from each sample. First, we validate our proteomics data and find a twofold reduction of
353 neuroproteasome surface expression in AD patients compared to controls in the BA7 region (**Fig**
354 **3D**). Moreover, we find a statistically significant reduction in neuroproteasome localization from
355 ApoE4/4 tissue compared to ApoE3/3 unaffected tissue (**Fig 3D**). In contrast, we do not observe
356 changes in total expression of the 20S proteasome from the cytosolic fraction, suggesting that the
357 ApoE-isoform dependent changes we observe are specific to neuroproteasome localization and
358 not a change in cytosolic proteasome levels. We find changes in Lrp1 concordant with that
359 observed with neuroproteasomes (**Fig S3A**). However, given the strong effect of AD pathology
360 on the global proteome (as well as on neuroproteasome localization), we next used the BA4
361 tissue to understand how ApoE isoforms could influence neuroproteasome localization with mild
362 AD pathology.

363

364 In BA4 tissue, unlike BA7, we find comparable surface localization of neuroproteasomes
365 between patients with and without AD (**Fig 3E**, **Fig S3B**). However, once stratified by ApoE
366 genotype, we find that ApoE4/4 patients have a nearly 50% reduction in surface localization of
367 neuroproteasome compared with ApoE3/3 patients (**Fig 3E**). Both of these conclusions are
368 supported by analysis of proteasome subunits from unbiased proteomics datasets from BA4
369 tissue (**Table S2**). Consistent with these observations, using LLVY degradation experiments to
370 measure the catalytic activity of the proteasome, we found a significant reduction in
371 neuroproteasome activity in AD samples compared to unaffected controls and no change in
372 cytosolic proteasome activity (**Fig S3C**). This demonstrates that ApoE4 can influence
373 neuroproteasome localization in areas with mild AD pathology. Taken together, we make two
374 conclusions based on these data: 1) that neuroproteasome localization is reduced in brain regions
375 which have increased susceptibility to AD pathology and 2) that ApoE4 reduces
376 neuroproteasome localization compared to ApoE3.
377

378

379 **Quantitative proteomics reveals that selective inhibition of neuroproteasomes induces 380 accumulation of sarkosyl-insoluble Tau**

381

382 What is the consequence of ApoE4-dependent reduction in neuroproteasome function, or more
383 broadly, any reduction in neuroproteasome function? The most straightforward way to address
384 this question is to leverage neuroproteasome-specific inhibitors. We previously accomplished
385 neuroproteasome-specific inhibition using Biotin-Epoxomicin: an analog of the covalent and
386 highly selective proteasome inhibitor Epoxomicin with an N-terminal Biotin moiety. This small
387 modification renders Biotin-Epoxomicin cell-impermeable for up to an hour and does not change
388 the selectivity or potency of Epoxomicin (4) (81-84). While time-limited, this approach found
389 that generally, neuroproteasome substrates are co- or peri-translationally degraded and that flux
390 through the neuroproteasome depends on neuronal activity(3, 4). However, the previous version
391 of Biotin-Epoxomicin was not a usable tool to assess broad physiological functions of
392 neuroproteasomes because the timescale was far too short and could not be used *in vivo*.
393

394

395 Based on principles of drug design, we considered that introducing a longer PEG linker between
396 the N-terminus of Epoxomicin and biotin would decrease the permeability of biotin-epoxomicin
397 and allow us to reveal long-term consequences of neuroproteasome inhibition(85, 86). We chose
398 Epoxomicin because it leverages the unique chemistry of the catalytic threonines of the
399 proteasome – the α -amino group of the threonine opens the epoxide of Epoxomicin which forms
400 the final covalent morpholino adduct. The catalytic residues of Serine and Cysteine proteases do
401 not have α -amino groups, which is the principle that renders Epoxomicin completely specific
402 both against its target and relative to other proteasome inhibitors. These advantages explain why
403 dozens of analogs of Epoxomicin have been made to the N-terminus without altering the
404 specificity of the drug against the proteasome: no off-target effects of Epoxomicin or its analogs

403 have been found in the two decades since its discovery (83, 84, 87-89). We synthesized click-
404 able analogs of Epoxomicin (Azide-Epoxomicin) that would allow us to append a broad range of
405 linkers (**Fig 4A**). We then conjugated Biotin-PEG24-Alkyne to Epoxomicin, producing Biotin-
406 PEG24-Epoxomicin, or iBEp (**Fig 4A**). We observe efficient conjugation by HPLC analysis (**Fig**
407 **S4A, B, C, D**). All molecules were HPLC-purified as single peaks and confirmed by LC/MS
408 analysis (**Fig S4D, E**).

409

410 We next tested the potency and selectivity of iBEp relative to Epoxomicin. Epoxomicin
411 covalently and irreversibly binds the catalytic β subunits of the proteasome – therefore, the biotin
412 moiety on iBEp serves as a tracer to detect whether proteasomes are inhibited by monitoring
413 biotin signal on an SDS-PAGE gel(83, 87-89). We detect covalent biotinylation of only three
414 proteins from iBEp-treated neurons, corresponding to the three catalytic subunits of the
415 proteasome (**Fig S4F**). Therefore, we demonstrate that the iBEp linker does not modify the high
416 specificity of iBEp compared to Epoxomicin alone. This is supported by previous data that
417 modification of the non-reactive end of epoxomicin has been shown not to change the selectivity
418 of Epoxomicin for the proteasome(83, 87-89). While iBEp is still highly active against the
419 proteasome, we do find that the Biotin-PEG24 linker moderately reduces the efficacy of iBEp
420 relative to Epoxomicin (**Fig S4G**). We therefore chose doses of inhibitor where the effective
421 concentration of the inhibitor was similar to previous studies using Epoxomicin alone and well
422 within the acceptable range of efficacy given how potent Epoxomicin is as a proteasome
423 inhibitor.

424

425 To test the permeability of our compounds, we incubated primary cortical neurons with iBEp
426 over a time course and prepared both cytosolic and plasma membrane-enriched fractions.
427 Samples were immunoblotted and probed for cytosolic marker Actin and membrane protein
428 GluR1 to validate our fractionation (**Fig 4B**). We found specific biotin signal corresponding to
429 covalent inhibition of the proteasome by iBEp only in the membrane fraction, and not in the
430 cytosol, over a 24 hour incubation in primary neurons (**Fig 4B**). As an orthogonal measure of cell
431 penetrance, we tested whether the activity of cytosolic proteasomes was affected by iBEp
432 treatment. We subjected cytosolic and membrane fractions from iBEp-treated neurons to LLVY-
433 based proteasome activity assays. Cytosolic proteasome activity remains completely intact from
434 iBEp-treated neurons compared to DMSO controls, but proteasome activity in the membrane
435 fraction is almost entirely abrogated (**Fig 4C**). This suggests that neuroproteasomes are inhibited
436 following iBEp incubation but cytosolic proteasomes remain unaffected.

437

438 To further validate our neuroproteasome-specific inhibitors, we sought a cellular functional
439 readout of whether our cell-impermeant inhibitors affected cytosolic proteasomes. One of the
440 most penetrant and robust consequences of total proteasome inhibition is the induction of
441 autophagy as a cellular response mechanism to compensate for the lack of proteasomal
442 degradation(31-33, 90-92). To test this, we assayed three autophagy markers, p62 levels,

443 LC3bI/II ratios, and Ulk1 levels. Each are robust markers of different steps of autophagy. p62
444 has been demonstrated to be rapidly induced upon proteasome inhibition and LC3bI/II induction
445 is thought to be slower, while Ulk1 is important for early phagosome formation(93). Cytosolic
446 proteasome inhibition has been reproducibly demonstrated to induce a strong increase in p62
447 levels in neurons(31, 32, 34, 93). Consistent with these reported observations, we find a strong
448 induction of p62 and little to no change in LC3bI/II following 12 hours of total proteasome
449 inhibition with epoxomicin (**Fig 4D**). However, when we treat primary neurons with iBEp, we
450 observe no change in either p62 or LC3bI/II levels (**Fig 4D**). These data are a functional
451 demonstration that iBEp is cell-impermeable to neurons and signify that specifically inhibiting
452 neuroproteasomes over all proteasomes does not induce compensatory autophagic degradation,
453 and together, validate the use of iBEp as a neuroproteasome-specific inhibitor.
454

455 One important advantage of iBEp is the ability to use over extended timecourses, a property
456 necessary to understand how neuroproteasomes shape the proteome, if at all. We hypothesized
457 that prolonged neuroproteasome inhibition may reveal not only the turnover of candidate
458 substrates, but also affect the solubility and aggregation of proteins. If true, this observation may
459 provide some explanatory power for how neuroproteasome dysfunction (driven by ApoE4 or
460 other mechanisms) could underlie deficits in proteostasis with potential relevance for
461 neurodegenerative disorders. We incubated DIV12-14 primary cortical neurons with cell-
462 impermeable proteasome inhibitors in biological duplicate for 1 and 6 hours, prepared sarkosyl-
463 soluble and sarkosyl-insoluble samples, and then collected and processed samples for
464 quantitative TMT-based proteomics (**Fig 4E**). We first analyzed proteins which increase over the
465 time-course in the soluble fraction. We recapitulate our previously published data and find that
466 neuroproteasome inhibition induces the accumulation of previously reported neuroproteasome
467 substrates such as Rgs4, c-Fos, Sox4, Snurf, Arc, and Bex2 in the soluble fraction (**Fig 4F, G**,
468 **Table S3**)(4). Importantly, we also do not see accumulation of classical ubiquitin-proteasome
469 substrates such as PSD-95, Homer1, or GKAP(94-96) (**Fig 4G**). We also fail to observe an
470 increase in p62, LC3b, GabarapL1, or any other marker of autophagy(1, 97) (**Fig 4G**). This
471 provides orthogonal evidence that iBEp does not detectably penetrate cells and demonstrates the
472 validity of this approach to determine the consequences of selective neuroproteasome inhibition.
473 These validate our previous data identifying neuroproteasome substrates(4) and extend them by
474 demonstrating neuroproteasome-dependent substrate turnover in a context without modulating
475 neuronal activity and over extended periods of time.
476

477 Next, our quantitative proteomics analysis revealed a selective pattern of protein insolubility
478 following neuroproteasome inhibition. We find that only 52 proteins become sarkosyl-insoluble
479 in response to neuroproteasome inhibition (**Fig 4H, Table S3**), in contrast with over 250 proteins
480 increasing in the soluble fraction (**Fig 4F**). To narrow in on this list, we quantitated which
481 proteins show a greater than log-fold change in the insoluble fraction, but showed no change in
482 the soluble fraction (**Fig 4I**). This analysis identified only four proteins which show significant

483 increases in the insoluble fraction relative to the soluble fraction (Ckmt1, Tau, Taf15, and
484 Hspb1) and one protein which significantly increases in the soluble fraction and showed no
485 change in the insoluble fraction (Plk2) (**Fig 4I**). Of note, Taf15 has previously been observed in
486 detergent-insoluble fractions of brains from Alzheimer's patients, correlated with both Amyloid
487 β and Tau insolubility(98-101). Ckmt1 has also been found in Neurofibrillary tangles and
488 interacting with phosphorylated Tau inclusions(102-104).

489

490 **Neuroproteasomes are differentially regulated by ApoE isoforms to determine formation of** 491 **endogenous sarkosyl-insoluble Tau inclusions**

492

493 Our findings raise the intriguing possibility that a fraction of endogenous mouse Tau becomes
494 sarkosyl-insoluble following neuroproteasome inhibition. We sought to validate these findings
495 by immunoblot and extend them to determine if the same principle would hold for human Tau
496 isoforms, without pathogenic and aggregation-driving mutations. We therefore cultured primary
497 mouse cortical neurons from either WT or hTau-KI mice (105). The entire mouse *Mapt* sequence
498 is replaced with the human *Mapt* sequence (including upstream gene regulatory elements) at the
499 endogenous locus in hTau-KI mice. hTau-KI mice express all six human isoforms of Tau protein
500 using the endogenous *Mapt* regulatory elements and therefore, hTau is expressed at normal
501 physiological levels(105). DIV12-14 neurons were treated with either the neuroproteasome
502 inhibitor iBEp or the cell-permeable proteasome inhibitor Epoxomicin. We then performed
503 sarkosyl fractionations to separate treated neurons into soluble and insoluble fractions and
504 immunoblotted these fractions for total Tau and GAPDH. The R2295 antibody reacts against
505 both total human and total mouse Tau and is highly specific, making it the ideal tool to monitor
506 endogenous Tau in WT and hTau-KI samples(106). We observed no Tau signal in primary
507 neurons cultured from Tau knockout (Tau-KO) mice, demonstrating the specificity of our
508 antibodies and approach (**Fig S5A**)(106). We found a significant increase in sarkosyl-insoluble
509 Tau from both the WT (**Fig 5A**) and hTau-KI neurons treated with iBEp (**Fig 5B, S5B**).
510 Intriguingly, we find no change in sarkosyl-insoluble Tau in neurons treated with the cell-
511 permeable Epoxomicin compared to DMSO controls, despite the fact that Epoxomicin inhibits
512 cytosolic proteasomes and neuroproteasomes (**Fig 5A,B**). We reason that Epoxomicin inhibits
513 neuroproteasomes and likely induces the formation of Tau inclusions (similar to iBEp), but these
514 Tau inclusions cannot be detected because simultaneous inhibition of cytosolic proteasomes
515 induces autophagy and other compensatory mechanisms which can clear these inclusions. This
516 claim is supported by an extensive body of work on Tau clearance mechanisms(31-35, 93). We
517 posit that such compensatory mechanisms are not triggered when neuroproteasomes are
518 specifically inhibited, which is consistent with our observations that Epoxomicin induces p62
519 expression whereas iBEp does not (**Fig 4D, G**).

520

521 Many of our experiments rely on the use of iBEp because the biotin tracer on an irreversible and
522 specific inhibitor allows us to track which proteasomes are inhibited. However, we wanted to

523 validate our findings using a proteasome inhibitor with a distinct mechanism of action from
524 Epoxomicin. We therefore modified MG132, a reversible peptide aldehyde proteasome inhibitor,
525 with a sulfonated biotin linker on the nonreactive N-terminus(84). This negatively charged
526 water-soluble linker renders Sulfo-MG132 (SulfoMG) cell-impermeable, much like the historical
527 use of sulfonated linkers to perform surface biotinylation (**Fig 5C**). We observe efficient
528 conjugation by HPLC analysis (**Fig S5C, D**). All molecules were HPLC-purified as single peaks
529 and confirmed by LC/MS analysis (**Fig S5E, F**). We find significant inhibition of proteasomes
530 using SulfoMG despite the moderate loss of efficacy compared to MG132 as a consequence of
531 the linker (**Fig S5G**). MG132 is a reversible inhibitor and therefore, we cannot detect the
532 covalent modification of the proteasome subunits. Instead, we turned to cellular and functional
533 readouts of permeability. We found a similar induction of autophagy markers in neurons treated
534 with MG132 as with epoxomicin and a similar lack of induction with SulfoMG as with iBEP
535 (**Fig 5C**). Confident in its use as a chemically orthogonal cell-impermeable proteasome inhibitor,
536 we next incubated DIV13 primary hTau-KI neurons with SulfoMG. We find that SulfoMG
537 induces similar partitioning of hTau into the sarkosyl-insoluble fraction as iBEP (**Fig 5D**).
538 Moreover, we find that MG132, like Epoxomicin, does not affect the sarkosyl-insoluble
539 accumulation of Tau (**Fig 5D**).
540

541 Next, we examined whether neuroproteasome inhibition would induce sarkosyl-insoluble
542 endogenous Tau inclusions *in vivo*. Here, we only used iBEP and not SulfoMG for three reasons:
543 first, because SulfoMG is reversible and is therefore subject to being washed out by CSF flow *in*
544 *vivo*; second, because we could biochemically monitor iBEP permeability using the presence of
545 the biotin signal; and third, because Epoxomicin is a more specific proteasome inhibitor than
546 MG132. We tested iBEP permeability *in vivo* by stereotactically injecting iBEP into the CA1
547 region of the mouse hippocampus for 72 hours. Hippocampi were microdissected and separated
548 into cytosolic and membrane-enriched fractions and samples were immunoblotted (**Fig 5E**). We
549 fail to observe penetration into the cytosol until we inject 64 μ M, so we chose to inject at 10-fold
550 under this dose as our maximal concentration (**Fig 5E**). This *in vivo* dose is consistent with and
551 far lower than previous studies using Epoxomicin alone (9.0 and 13.5mM (107, 108)). We
552 performed stereotactic injections of 6.4 uM iBEP and contralateral injections of the vehicle
553 (0.07% DMSO) into the hippocampus of hTau-KI and Tau-KO mice. After 72 hours, we
554 collected the hippocampi and performed sarkosyl extractions into soluble and insoluble fractions.
555 We fail to observe any detectable Tau in the Tau-KO mice in DMSO- or iBEP-injected
556 hippocampi (**Fig S5H**). Mirroring our data in primary neurons, we find a strong increase of
557 sarkosyl-insoluble Tau in hippocampi from hTau-KI mice injected with iBEP (**Fig 5F**).
558

559 In our experiments, we find that inhibiting neuroproteasomes to saturation induces the
560 accumulation of sarkosyl-insoluble Tau. Taken together with our data demonstrating that ApoE
561 isoforms regulate neuroproteasome localization (ApoE4<E3<E2), we predicted that neurons
562 from ApoE4-KI mice would be more susceptible accumulating sarkosyl-insoluble Tau relative to

563 neurons from ApoE3-KI or ApoE2-KI mice. To test this prediction, we crossed each of the
564 ApoE-KI lines to the hTau-KI lines, generating mice which endogenously express ApoE2, E3, or
565 E4 as well as hTau. DIV14 primary neurons from each line (hTau/ApoE2 double KI,
566 hTau/ApoE3 double KI, and hTau/ApoE4 double KI) were then treated with a range of iBEp
567 doses spanning four log units. Neurons were then separated into sarkosyl-soluble and insoluble
568 fractions and immunoblotted. We found no sarkosyl-insoluble Tau aggregates at baseline in any
569 line, which suggests that the ApoE4-induced reduction of neuroproteasomes levels alone is not
570 sufficient to drive Tau aggregation (**Fig 5G, S5I**). However, after treatment with even the lowest
571 dose of iBEp, we found accumulation of sarkosyl-insoluble Tau in hTau/E4-dKI neurons,
572 rendering E4 neurons over 25-fold more susceptible to Tau aggregation than E3 neurons (**Fig**
573 **5G**). Conversely, neurons from hTau/E2-dKI mice were over 10-fold less susceptible to
574 neuroproteasome-inhibition induced Tau aggregation than neurons from hTau/E3-dKI mice (**Fig**
575 **5G**). Overall, these data demonstrate that ApoE isoforms differentially shift the threshold for the
576 neuroproteasome-dependent formation of endogenous sarkosyl-insoluble Tau inclusions.
577

578 **Neuroproteasome inhibition induces endogenous phosphorylated, sarkosyl-insoluble,**
579 **Thioflavin S-positive Tau aggregates**

580 We noticed that neuroproteasome inhibition induces the shift of sarkosyl-insoluble Tau into a
581 species which migrates at a higher molecular weight on an SDS-PAGE gel, at approximately
582 64kDa (**Fig 5A, B, D, F, G, S5B, S6A**). Similar shifts in molecular weight of Tau are observed
583 in the AD brain and is a hallmark phenotype of multiple neurodegenerative disorders (109, 110).
584 This molecular weight shift can in part be due to Tau phosphorylation at many residues.
585 Therefore, we wanted to address whether iBEp-induced Tau aggregates are phosphorylated.
586 Rather than profiling by a panel of phospho-specific antibodies against Tau, we took a more
587 unbiased approach and measured Tau phosphorylation by quantitative phosphoproteomics. We
588 treated primary WT neurons with iBEp for either 1, 6, or 24 hours and then performed sarkosyl
589 fractionations. Soluble and insoluble fractions were processed for TMT labelling in preparation
590 for quantitative mass spectrometry and then peptides were run over an Fe-NTA column to enrich
591 for phospho-peptides (**Fig 6A**). We then used this enriched population for quantitative phospho-
592 proteomics analysis at the single peptide level (**Table S4**). Here, we find a time-dependent
593 increase in Tau phosphorylation at only 4 of 26 identified sites which correspond to human S202,
594 T205, T217, and S404 (**Fig 6A**). This is a specific signature of phosphorylation which
595 corresponds to sites at which Tau is phosphorylated in the AD brain and detected by established
596 antibodies (S202 – CP13(111), T205 – AT8(112), and S404 – PHF1(113)) as well as CSF
597 biomarkers for AD progression (T217)(114).

598
599 To validate these data, we treated hTau-KI neurons with iBEp and then fixed and stained these
600 neurons. We observed no staining in neurons cultured from Tau-KO mice using the R2295
602 antibody to detect total Tau or the CP13 antibody to detect phosphorylated S202 (**Fig S6B**).

603 Incubating neurons with secondary antibodies alone showed no signal (**Fig S6C**). We therefore
604 exclusively used CP13 for our ICC experiments to detect phosphorylated Tau. We find a
605 significant elevation of CP13 signal in iBEP-treated primary hippocampal hTau-KI neurons
606 compared to controls (**Fig 6B**). This iBEP-induced signal appears punctate and distributed in
607 both axons and MAP2+ dendrites (**Fig 6B**). To validate these data, we conducted
608 immunohistochemical (IHC) analysis of sections from hTau-KI mice stereotactically injected
609 with iBEP and contralaterally injected with vehicle control (0.07% DMSO). After stereotactic
610 injections, animals were allowed to recover for 72 hours and then were perfused and sectioned
611 for IHC. We observed no staining in the Tau-KO mice using the AT8 antibody or with secondary
612 antibodies alone (**Fig S6D, S6E**). We observe a threefold induction of phosphorylated Tau signal
613 in hippocampi injected with iBEP compared to the contralateral PBS controls. We see a strong
614 increase in AT8+ inclusions mislocalized to somatodendritic compartments in iBEP-injected
615 hippocampi, which extend into the stratum radiatum and stratum moleculare (**Fig 6C**).
616

617 While sarkosyl-insoluble Tau reflects aggregated Tau species(99, 106, 115-117), there are
618 varying definitions of a protein aggregate: misfolded proteins which cluster together, proteins
619 which form stable inclusions, inclusions which are resistant to varying detergents, and then in
620 some cases, proteins which form very stable aggregates and even amyloids(118, 119). Thioflavin
621 S (ThioS) is a dye that stains the β -sheet structures of amyloid aggregates, including both
622 aggregated Tau tangles and amyloid plaques. Therefore, ThioS is used for the neuropathological
623 diagnosis of a wide variety of neurodegenerative disorders(8, 54, 120). We conducted ThioS
624 staining of sections from hTau-KI mice stereotactically injected with iBEP and contralaterally
625 injected with vehicle control. After stereotactic injections, animals were allowed to recover for
626 72 hours and then brains were perfused, sectioned, and stained for ThioS. We find a strong
627 increase in ThioS staining from the CA1 region of hippocampi exposed to iBEP relative to
628 vehicle controls (**Fig 6D**). ThioS+ inclusions appear as flame-like inclusions in both the CA1
629 pyramidal layer and the granule cell layer of the Dentate Gyrus (**Fig 6D, E, S6F-J**).
630 Neuroproteasome inhibition-induced flame-like ThioS+ aggregates co-localize with both
631 phosphorylated Tau (AT8) and total Tau (DA9) (**Fig 6F, G, S6K**) in single Z-plane images from
632 neurons in the CA1 and DG of hippocampus. We conclude that some neuroproteasome-induced
633 aggregates we observe are indeed composed of Tau. In addition to these large ThioS+ inclusions,
634 we also observe some thread-like ThioS+ inclusions in the hippocampal neuropil as well as
635 widely distributed thin ThioS+ inclusions that appear dispersely throughout the iBEP-injected
636 hippocampus (**Fig 6G, S6L, M**). The ThioS+ inclusions formed following neuroproteasome
637 inhibition appear to resemble neurofibrillary tangle (NFT)-like and neuropil thread-like
638 inclusions observed in various Tauopathies including AD (8, 17, 54, 120). While we find it
639 highly surprising that ThioS+ Tau inclusions appear just 72 hours after neuroproteasome
640 inhibition, these data support our overall conclusion that neuroproteasome inhibition induces the
641 aggregation of endogenous Tau.

642 ***De novo* protein synthesis is required for neuroproteasome-dependent induction of
643 endogenous Tau aggregates**

644

645 Neuroproteasomes are 20S complexes and do not have the machinery to recognize ubiquitin or
646 unfold substrates(3, 4). Instead, neuroproteasomes co- or peri-translationally degrade newly
647 synthesized and unfolded substrates rather than substrates which are fully folded(4). We
648 therefore tested whether new protein synthesis was required for the neuroproteasome-dependent
649 formation of endogenous Tau aggregates. We incubated primary neuronal cultures with either
650 iBEp or Epoxomicin and then co-incubated these cultures with cycloheximide, which blocks
651 translation elongation. Here, we reproduce iBEp-induced Tau aggregation and find that
652 cycloheximide blocks this iBEp-mediated increase in both WT primary neurons (**Fig 7A**) and in
653 hTau-KI primary neurons (**Fig 7B**). Cycloheximide also blocks the effect of SulfoMG on the
654 formation of endogenous insoluble Tau inclusions, consistent with our observations using iBEp
655 (**Fig 7C**). Next, we tested whether inhibition of protein synthesis blocks the accumulation of
656 sarkosyl-insoluble Tau *in vivo* in hTau-KI mice. We stereotactically co-injected cycloheximide
657 and iBEp together contralateral to iBEp alone into the hippocampus. We find a dramatic
658 decrease in sarkosyl-insoluble Tau in the hippocampus from mice co-injected with iBEp and
659 cycloheximide compared to those injected with iBEp alone (**Fig 7D, S7A**). Next, co-injection of
660 cycloheximide with iBEp completely eliminated AT8 staining compared to contralateral
661 injection of iBEp alone (**Fig 7E**). Finally, similar to what we observed with sarkosyl-insoluble
662 Tau and AT8 staining, we also observe a complete return to baseline of ThioS⁺ staining in
663 hippocampi co-injected with iBEp and cycloheximide relative to those injected with iBEp alone
664 (**Fig 7F**).

665

666 There are many mechanisms which could explain our observation that new protein synthesis is
667 required for the formation of neuroproteasome inhibition-induced endogenous Tau aggregates.
668 We interpret our data and argue that neuroproteasome inhibition induces the accumulation of
669 newly synthesized protein(s) important for Tau accumulation. The most straightforward
670 candidate protein would be Tau itself. To determine specifically if we observed more newly
671 synthesized Tau protein following neuroproteasome inhibition, we took advantage of proximity
672 ligation assays (PLA) coupled with puromycylation to visualize newly synthesized Tau
673 protein(121, 122). Briefly, we used specific monoclonal N-terminal antibodies against Tau and
674 specific antibodies against puromycin. Each antibody is recognized by secondary antibodies
675 tethered to oligonucleotides that can ligate and amplify *in situ*. When antibodies against Tau and
676 Puromycin are proximal to each other, this permits the oligonucleotide ligation which can be
677 detected by a fluorescent signal under hybridizing conditions (**Fig 7G**). A positive PLA signal
678 therefore indicates the presence of newly synthesized Tau. We incubated Puromycin in primary
679 neuronal cultures for only 10 minutes, which allows us to visualize a defined short snapshot of
680 newly synthesized Tau. We observe no signal in neurons either not treated with puromycin or in
681 neurons where we block protein synthesis using cycloheximide or anisomycin during

682 puromycylation, validating our approach (**Fig S7B, C**). We observe a striking ~3.5-fold increase
683 in Puro-PLA-Tau signal in iBEp-treated neurons relative to DMSO controls (**Fig 7H**). We then
684 analyzed the size distribution of diameters of the newly synthesized Tau puncta (**Fig 7I**). After
685 accounting for and normalizing against the increase in puncta number seen in iBEp-treated
686 neurons, we observe an increase in the size distribution of PLA puncta from iBEp treated
687 neurons. We find that iBEp treated neurons contain an over twofold increase in newly
688 synthesized Tau puncta greater than 24nm in diameter (**Fig 7I**). We interpret this to mean that
689 there are larger inclusions of newly synthesized Tau which form following neuroproteasome
690 inhibition, consistent with our observations that neuroproteasome inhibition induces Tau
691 aggregation.
692

693 Discussion

694

695 We conclude that neuroproteasome localization is differentially regulated by ApoE isoforms,
696 which is critically important because reduced neuroproteasome function induces the aggregation
697 of endogenous Tau. The relevance for neuroproteasomes in many aspects of the cell biology of
698 neurons, as well as pathophysiology of neurodegeneration, will be critical to explore in the
699 future. The cell-impermeable neuroproteasome-specific inhibitors we have developed and the
700 tools we have built to visualize and purify neuroproteasomes will enable the broad study of
701 neuroproteasomes in various aspects of neuronal physiology and pathophysiology.
702

703 The mechanisms by which ApoE interacts with and influences neuroproteasome localization
704 remain unexplored. ApoE is found as a lipoprotein and the classic role for ApoE is a cholesterol
705 carrier(123). While we demonstrate only lipidated ApoE can influence neuroproteasome
706 localization, we do not understand whether the lipids transported by ApoE are involved in
707 regulating neuroproteasomes or if the lipoproteins are more efficiently able to interact with the
708 neuroproteasome complex. Neuroproteasome levels change in ApoE3/3 AD carriers relative to
709 controls, which likely suggests that other mechanisms besides ApoE are at play in controlling
710 neuroproteasome localization. It is therefore an open and important task to define the milieu of
711 molecular and cell biological factors that can influence neuroproteasome localization. Detailed
712 characterization of such mechanisms may help understand whether and how neuroproteasomes
713 contribute to the large diversity of phenotypes in Tauopathies and neurodegenerative disease.
714 Along these lines, ApoE has large effects on both amyloid deposition and Tau aggregation based
715 on neuropathological data (124). Future work will determine whether and how neuroproteasomes
716 can impinge on the amyloid pathway, if at all.
717

718 In the broadest sense, we find that neuroproteasome localization and function is a determinant
719 for the proteostatic capacity of neurons to defend against protein aggregation. A major
720 conclusion of our work is that neuroproteasome-specific inhibition induces the formation of
721 endogenous Tau inclusions, suggesting the neuroproteasome is a pivotal mechanism in

722 determining Tau aggregate formation. This function is notably distinct from the canonical role of
723 proteasomes in protein clearance. Sarkosyl-insoluble Tau aggregates formed by neuroproteasome
724 inhibition in neurons are endogenous, without a need for pathogenic mutations. We suggest that
725 this may be important for Tau aggregation observed in a high percentage of sporadic AD patients
726 who do not have genetic lesions in the *MAPT* locus. It will likely be important to determine how
727 neuroproteasome inhibition-induced endogenous Tau aggregates compare to other types of
728 misfolded Tau.

729

730 One of the key observations we make is that new protein synthesis is necessary for
731 neuroproteasome-inhibition induced Tau aggregation. Taken together with the dramatic increase
732 in newly synthesized Tau protein following neuroproteasome inhibition, we propose two models
733 to explain our observations (**Fig S7D**): one, that neuroproteasomes degrade newly synthesized
734 Tau, or two, that neuroproteasomes indirectly regulate the translation machinery itself. The latter
735 is unlikely because only ~500 proteins increase after neuroproteasome inhibition, which suggests
736 some degree of specificity of what is regulated by neuroproteasomes. Based on the small number
737 of neuroproteasome substrates (4) and even smaller number of proteins which we identify in this
738 study which become insoluble, we suggest that the model that neuroproteasomes degrade Tau to
739 be the most likely option. While further experiments are needed to determine which is accurate,
740 our observation that newly synthesized and endogenous Tau forms aggregates following
741 neuroproteasome inhibition is likely to be an important finding for the field. Indeed, if newly
742 synthesized Tau is a neuroproteasome substrate, future analysis would determine if Tau
743 mutations or Tau seeding would perturb the balance of protein synthesis and degradation. This
744 would be an important cautionary consideration for using these common models to study
745 neuroproteasome-dependent Tau aggregation.

746

747 As a concluding note, our findings increase the urgency to understand fundamental aspects of
748 neuroproteasome biology. For example, revealing the genetic and cell biological elements which
749 control neuroproteasome localization and trafficking are likely to be critical to reveal how ApoE
750 exerts an effect on neuroproteasome localization. The majority of the other components
751 identified are involved in synaptic vesicle recycling and membrane trafficking (NSF, COPI,
752 Vps35 and Sor11, AP2 and AP3). We believe this reflects the underlying cellular mechanisms for
753 regulating localization of these complexes to the plasma membrane, a subject for future study.
754 Understanding these, as well as related mechanisms like how newly synthesized proteins are
755 degraded by neuroproteasomes, are likely to open up therapeutic avenues that can impinge on
756 neuroproteasome biology to boost neuroproteasome dependent-proteostasis and delay or prevent
757 protein aggregation.

758

759

760

761

762 **Acknowledgements**

763

764 We thank the families and patients who contributed human tissue which enabled the discoveries
765 in this manuscript. We thank Peter Davies for the DA9 antibody and Virginia Lee for the R2295
766 antibody. We thank Abid Hussaini for providing the hTau-KI mice and Carol Troy for the
767 perfusion setup. We thank Claire Chen for IHC training, Ottavio Arancio and Elentina Argyrousi
768 for stereotactic surgery training, and Reiji Kuruvilla and Guillermo Moya Alvarado for technical
769 assistance with the FLAG antibody feeding experiments. We also thank Leona Lee for help with
770 plasmid sequence alignments. We thank Ulrich Hengst and Clarissa Waites for discussions, Leah
771 Cairns, Nikhil Sharma, Franck Polleux, and Lloyd Greene for careful reading and comments, and
772 Sadie for invaluable laboratory support. We also thank Michael Shelanski, Richard Mayeux, and
773 the Taub Institute for support and start-up funding. We thank the Thermo Fisher Scientific
774 Center for Multiplexed Proteomics at Harvard Medical School (<http://tcmp.hms.edu>).
775

776

777 **Funding Sources**

778

779 KVR supported by NIH Director's Early Independence Award v, Department of Defense
780 CDMRP award W81XWH-21-1-0093, Fidelity Biomedical Research Initiative, Norm
781 Foundation Impetus Grants, Startup funding from Columbia University: Taub Institute, Eli Lilly,
782 MassCATS award, American Federation for Aging Research New Investigator Grant, and the
783 Harvard Milton Fund. DMH supported by RF1AG047644, R01S090934, and The JPB
784 Foundation. Human samples obtained from the Massachusetts General Hospital ADRC funded
785 by P30AG062421.
786

787

788 **Author Contributions**

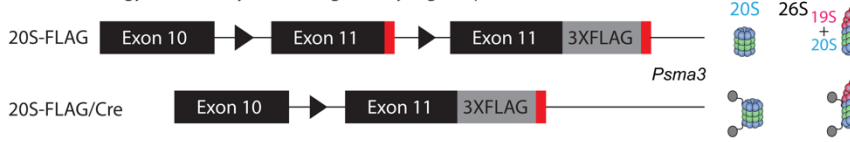
789

790 KVR conceptualized the project and KVR and VP designed the methodology for all experiments.
791 VP performed the majority of experiments. In addition, MS performed all stereotactic injections
792 and in vivo surgeries, JB performed the proteomic screen in mice, NAS and CN designed and
793 synthesized neuroproteasome-specific inhibitors, RM performed the majority of the IHC
794 sectioning and produced primary embryonic cultures, KDKV performed all Puro-PLA
795 experiments and analysis, XW performed proteasome isolations, JF analyzed proteomic datasets,
796 BTC performed blinded ThioS quantification, JN helped arrange figures, GM performed
797 perfusion experiments for ApoE-TR experiments and blinded experimenters and trained MS in
798 stereotactic surgeries, MSt prepared lipidated ApoE particles, HF maintained mouse crosses,
799 DA, JN, XW, RM, CN, MS, and VP aided with writing and KVR did the majority of writing. BH
800 provided ApoE human postmortem samples and important insights, DMH provided reagents for
801 the in vitro lipidated ApoE experiments and important insights, and TN provided ApoE2, 3, and
802 4-KI mice as well as hTau/ApoE2, 3, and 4 double KI mice. KVR was responsible for acquiring
803 funding and supervised the project.
804

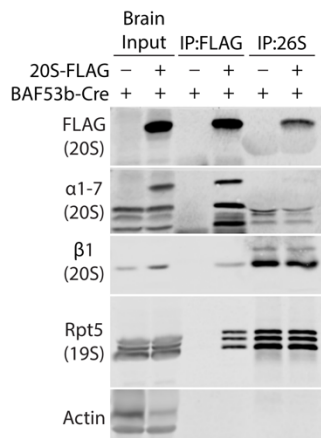
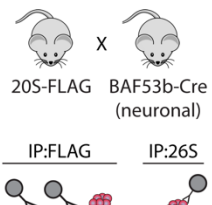
802

Figures

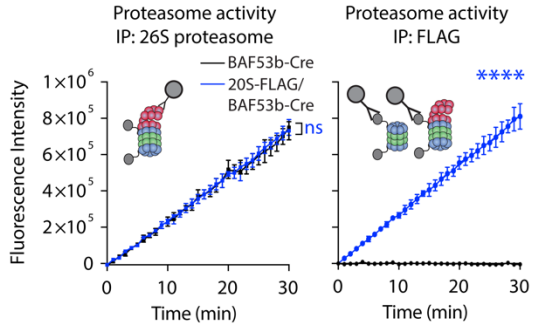
A Genetic strategy to inducibly and endogenously tag the proteasome



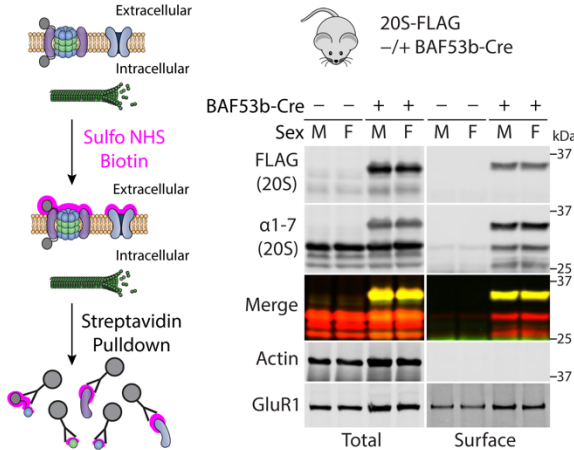
B



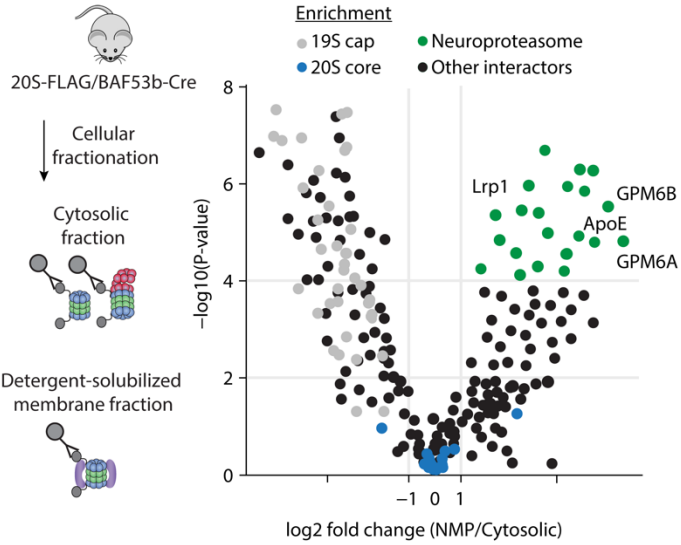
C



D



E



F

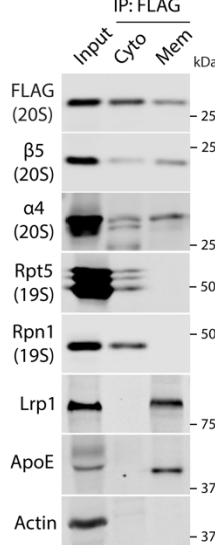


Figure 1
Paradise et al, 2023

804 **Figure 1: Neuroproteasomes co-purify with ApoE and Lrp1**

805

806 **(A)** Schematic for endogenous and conditional tagging of the 20S proteasome with FLAG tag.
807 (Top) Schematic of *Psma3* gene locus, endogenous Exon 11 containing the stop codon (red
808 rectangle) was flanked with loxP sites (black triangles), and an insert containing 3x-FLAG
809 tagged Exon 11 (gray) was inserted into the 3' UTR of the gene. Transgene referred to as 20S-
810 FLAG. (Bottom) Diagram of 20S-FLAG/Cre: in the presence of Cre, the native Exon 11
811 containing the stop codon was excised, driving the expression of FLAG tag from the endogenous
812 *Psma3* locus. (Right, top) Schematics of proteasome complexes: 20S and 26S (20S + 19S
813 regulatory particle). (Right, bottom) Schematics of proteasome complexes with 20S-FLAG tag
814 (gray circles) after Cre recombination.

815

816 **(B)** Proteasome purifications from the cytosol of brains from 20S-FLAG/BAF53b-Cre mice.
817 (Top) 20S-FLAG mice crossed with pan-neuronal Cre driver line BAF53b-Cre to induce 20S-
818 FLAG expression in neurons. (Middle) Diagram of proteasomal complexes isolated by different
819 affinity methods; Immunoprecipitation (IP) using FLAG beads isolate FLAG-tagged 20S core
820 particle as well as the 20S-containing 26S particle, whereas IP against the 19S only isolates 26S
821 particles. (Bottom) FLAG and 26S IP from mouse brain cytosolic fractions immunoblotted using
822 indicated antibodies.

823

824 **(C)** Comparison of FLAG-20S proteasomes with unmodified native proteasomes. Catalytic
825 activity of proteasomes isolated by 26S IP (left) and FLAG IP (right) from whole brain cytosol.
826 Proteasomes were isolated as in (b) from BAF53b-Cre mice (black) or 20S-FLAG/BAF53b-Cre
827 mice (blue). Catalytic activity of isolated proteasomes was measured by monitoring cleavage of
828 model substrate, Suc-LLVY-AMC. Proteasome-dependent cleavage of the substrate increases
829 AMC fluorescence. Data are mean ± SEM from three biological replicates. ***<0.0001 by
830 Two-Way ANOVA.

831

832 **(D)** Surface biotinylation to isolate surface-exposed proteins from 20S-FLAG/BAF53b-Cre
833 hippocampi. (Left) Diagram of surface biotinylation and streptavidin pulldowns.
834 Neuroproteasomes (20S surrounded by purple accessory proteins) and other membrane proteins
835 (blue) depicted in membrane, cytosolic proteins such as microtubules (green) in intracellular
836 space. Hippocampal tissues from 20S-FLAG mice alone or with BAF53b-Cre were dissected and
837 subjected to surface biotinylation using amine-reactive sulfo-NHS-biotin (pink). Lysates
838 incubated with streptavidin beads to pull down surface-exposed proteins. (Right) 20S proteasome
839 signal in surface pulldown denotes the neuroproteasome. Streptavidin pulldown of surface
840 proteins in 20S-FLAG male (M) or female (F) mice, -/+ BAF53b-Cre. Lysates (Total) and
841 Streptavidin pulldowns (Surface) immunoblotted using indicated antibodies against the FLAG
842 epitope tag, the 20S proteasome (α 1-7), a cytosolic protein (Actin), and a membrane protein
843 (GluR1). Merge indicates overlay (yellow) between FLAG (green) and α 1-7 blots (red).

844

845 **(E)** Co-IP and mass spectrometry (MS) analysis of 20S-FLAG proteasomes from cytosolic and
846 membrane-enriched fractions. (Left) Cytosolic and membrane fractions were prepared from
847 whole brains of 20S-FLAG/BAF53b-Cre and immunoprecipitates were isolated using anti-
848 FLAG affinity beads. (Right) Samples were subjected to tandem mass tag (TMT) labeling and
849 quantitative mass spectrometry. Differential levels of proteins enriched with membrane-
850 associated neuroproteasomes vs. cytosolic proteasomes were analyzed and plotted as log2-fold
851 change vs $-\log_{10}(P\text{-value})$. Green dots represent proteins enriched in the neuroproteasome IP,
852 blue dots represent 20S core subunits, and gray dots represent proteins in 19S cap.
853

854 **(F)** Validation of Co-IP proteomics data. 20S-FLAG Co-IP from cytosolic (cyto) and membrane
855 (mem) fractions of 20S-FLAG/BAF53b-Cre mouse brain tissue (inputs). Fractions were
856 immunoblotted using indicated antibodies.

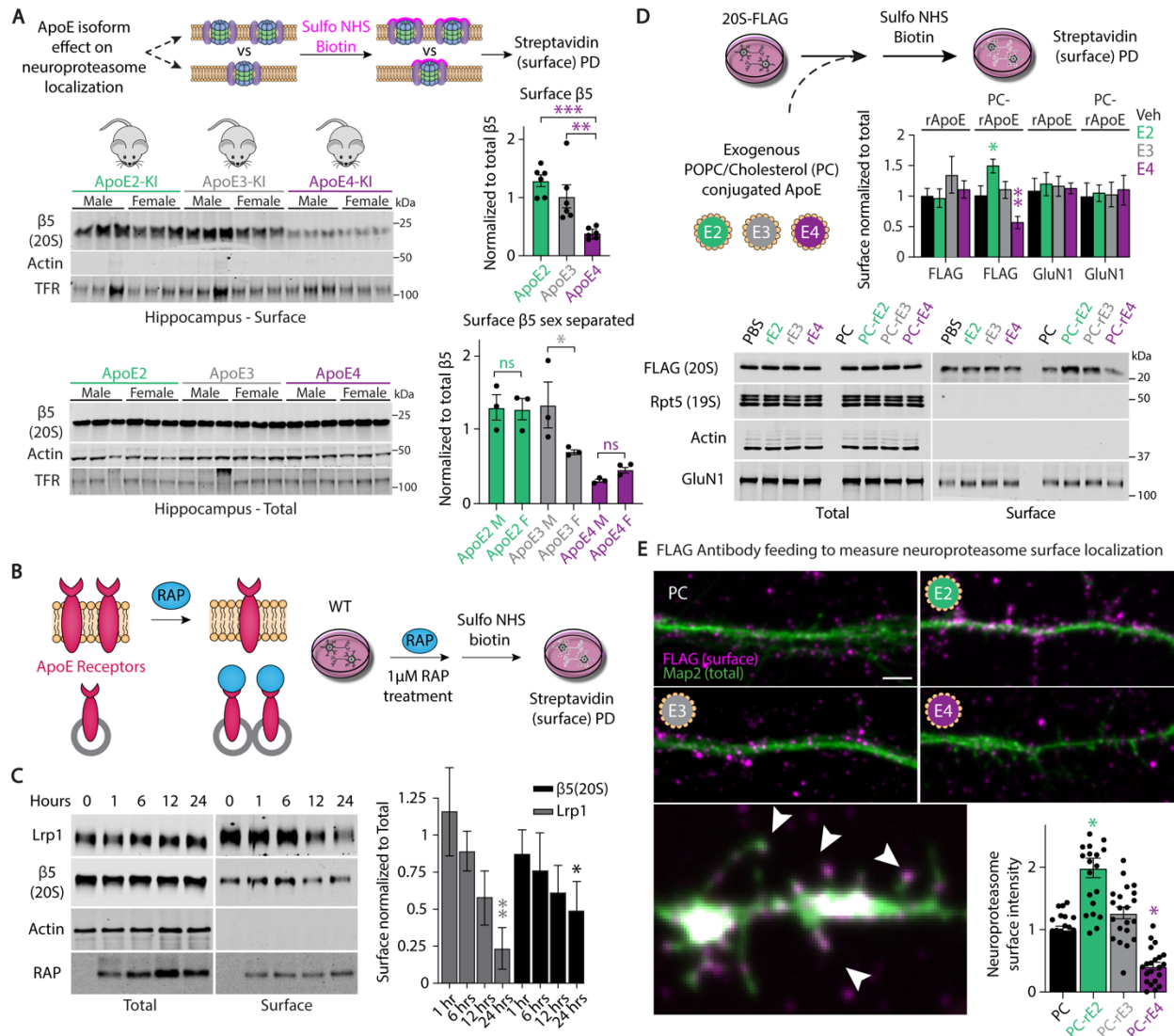


Figure 2
Paradise et al, 2023

857

858

859 **Figure 2: ApoE isoforms differentially modulate neuroproteasome localization in primary**
860 **neurons and *in vivo***

861

862

(A) Surface biotinylation of hippocampi from hApoE-KI mice to assess neuroproteasome localization. Schematic (top) of surface biotinylation experiments from ApoE isoform knock-in (ApoE 2, 3, or 4-KI) mice to determine if neuroproteasome localization changes with ApoE genotype. Hippocampi (hippo) from ApoE2-KI (green), ApoE3-KI (gray), and ApoE4-KI (purple), male (M) and female (F) mice were subjected to surface biotinylation and streptavidin pulldown to isolate surface exposed proteins. Experimenters were blinded to genotype. Lysates (Total) and Streptavidin pulldowns (Surface) were immunoblotted using indicated antibodies. Quantification of surface β5 intensity was normalized to total β5 intensity. Data (right) are mean

870 ± SEM normalized to ApoE3-KI, N=6 biological replicates per genotype (3 M, 3 F),
871 ***p<0.001, **p<0.01 by One-Way ANOVA, *p<0.05 by Two-Way ANOVA Tukey's Multiple
872 Comparisons Test.

873
874 **(B,C)** **(B)** Schematic of surface biotinylation of Receptor-Associated Protein (RAP)-treated
875 neurons. Influence of RAP (blue) on surface ApoE receptors (light red) is depicted. Gray circles
876 represent endosomes. **(C)** DIV13-14 primary cortical neurons obtained from WT mice were
877 treated with 1 μ M RAP for indicated time subjected to surface biotinylation. 20S proteasome
878 signal in surface pulldown denotes the neuroproteasome. Lysates (Total) and Streptavidin
879 pulldowns (Surface) were immunoblotted using indicated antibodies. Quantification of surface
880 Lrp1 and β 5 intensity was normalized to corresponding total signal. Data (right) are mean ± SEM
881 normalized to 0 hr condition. N=3 biological replicates, **p<0.01, *p<0.05 by One-Way
882 ANOVA Tukey's Multiple Comparisons Test.

883
884 **(D)** Surface biotinylation of 20S-FLAG neurons treated with exogenous ApoE isoforms (top
885 left). DIV2 primary cortical neurons from 20S-FLAG mice were transduced with Cre AAVs to
886 drive 20S-FLAG transgene expression. At DIV13, neurons were treated with exogenous
887 unconjugated recombinant ApoE isoforms (400 nM; rE2: green; rE3: gray; rE4: purple), or
888 POPC/Cholesterol (PC)-conjugated (yellow shell) recombinant ApoE isoforms (400nM; PC-rE2:
889 green; PC-rE3: gray; PC-rE4: purple) for 24 hours and subjected to surface biotinylation. Lysates
890 (Total) and Streptavidin pulldowns (Surface) were immunoblotted using indicated antibodies.
891 Quantification of surface FLAG and GluN1 intensities were normalized to corresponding total
892 intensities. Data (above) are mean ± SEM normalized to corresponding vehicle control. N=3
893 biological replicates, **p<0.01, *p<0.05 by One-Way ANOVA Tukey's Multiple Comparisons
894 Test.

895
896 **(E)** Antibody feeding of 20S-FLAG neurons treated with exogenous ApoE isoforms. DIV2
897 primary cortical neurons from 20S-FLAG mice were transduced with Cre AAVs to drive 20S-
898 FLAG transgene expression. At DIV13, neurons were treated with 400 nM PC-E2 (green), PC-
899 E3 (gray), and PC-E4 (purple) for 24 hours. FLAG antibodies were fed on live neurons to label
900 surface FLAG-neuroproteasomes (FLAG Surface). Subsequently, neurons were fixed and
901 stained for MAP2 (MAP2 Total). Quantification of surface FLAG fluorescence intensity was
902 normalized to total MAP2 fluorescence intensity. Data (below) are mean ± SEM normalized to
903 PC alone. N=3 biological replicates, n=21 quantified regions, *p<0.05 by One-Way ANOVA
904 Tukey's Multiple Comparisons Test. Scale bar=2 μ m.

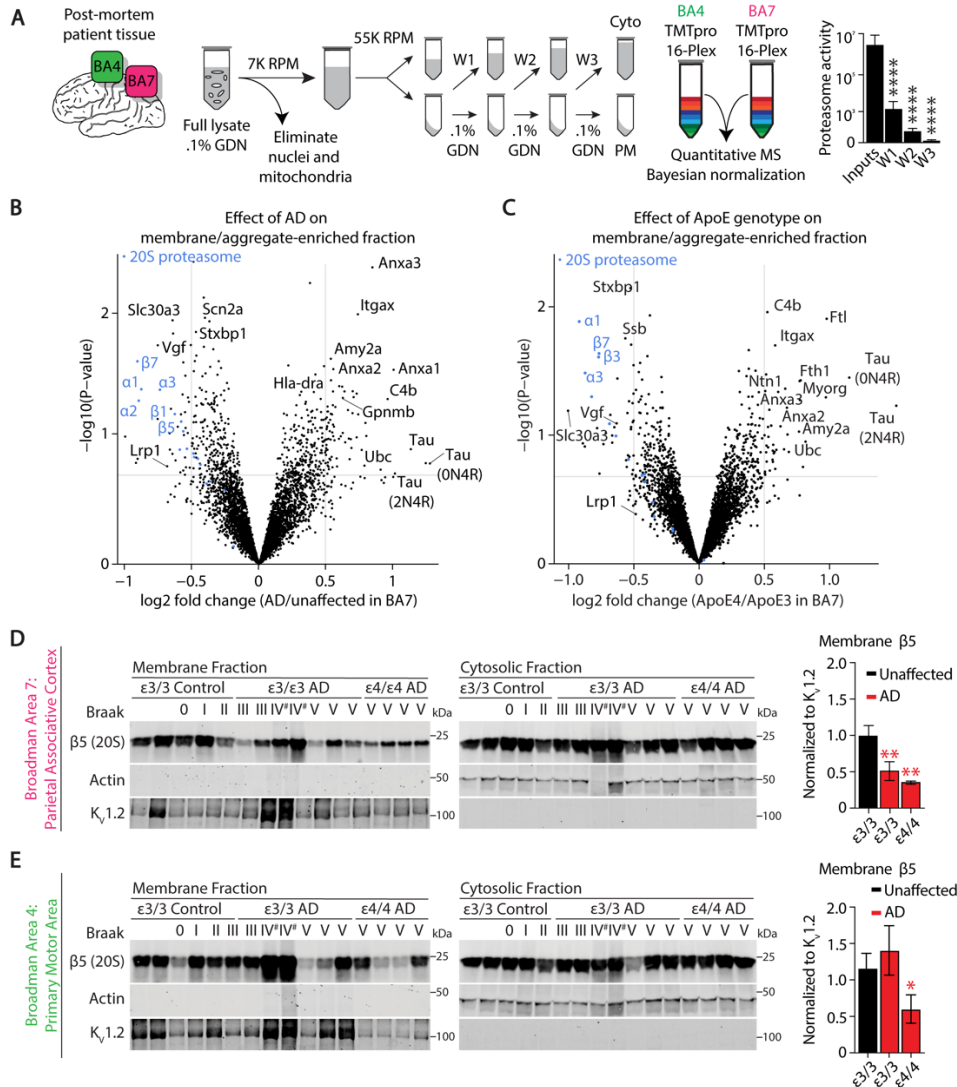


Figure 3
Paradise et al, 2023

905
906

907 **Figure 3: Neuroproteasome localization is reduced in AD-vulnerable brain regions in the**
908 **human brain and is further reduced by ApoE4 genotype**

909
910
911
912
913
914
915
916
917
918

(A) Schematic depicting steps to enrich plasma membranes from post-mortem human brain tissues. Post-mortem sections from Brodmann Area 7 (BA7, pink) and BA4 (green) were fractionated into crude membrane fractions, which were then washed 3 times (W1, W2, W3). Supernatants from washes were pooled to generate cytosolic fractions (Cyto). Membrane-enriched fractions also contain detergent insoluble protein (membrane/aggregate-enriched, PM). PM samples were labeled with Tandem Mass Tags (TMTpro) for quantitative MS. Cytosolic contamination assessed by the proteasome catalytic activity of the washes, graphed (right). N=32, ****p<0.0001 by Paired T-Test. Experimenters were blinded to sample identity.

919 **(B)** Determining effect of AD on the plasma membrane and detergent-insoluble proteome.
920 Differential enrichment of plasma membrane and detergent-insoluble proteins from BA7 of AD
921 vs. unaffected patients was analyzed and plotted as log₂-fold change vs -log₁₀(P-value). Blue
922 dots indicate 20S proteasome subunits, analysis was also done blinded to sample identity.
923
924 **(C)** Determining effect of ApoE genotype on the plasma membrane and detergent-insoluble
925 proteome. Differential enrichment of plasma membrane and detergent-insoluble proteins from
926 BA7 in Apoε4/4 vs Apoε3/3 patients was analyzed and plotted as log₂-fold change vs -log₁₀(P-
927 value). Blue dots indicate 20S proteasome subunits, analysis was also done blinded to sample
928 identity.
929
930 **(D)** Determining effect of AD and ApoE genotype on neuroproteasome membrane localization in
931 BA7 (pink). Membrane and cytosolic fractions from BA7 from Apoε3/3 patients with AD (AD)
932 and without AD (unaffected) and Apoε4/4 patients with AD were immunoblotted using indicated
933 antibodies. Braak stages indicated above. (Right) Quantification of membrane β5 intensities were
934 quantified and normalized to membrane loading control K_v1.2. Data (right) are mean ± SEM
935 normalized to ε3/3 unaffected. # indicates samples excluded from analysis on basis of high
936 abnormal actin and K_v1.2 signal. **p<0.01 by Two-Way ANOVA Fisher's LSD Test relative to
937 BA7 ε3/3 unaffected.
938
939 **(E)** Determining effect of AD and ApoE genotype on neuroproteasome membrane localization in
940 BA4 (green). Experimental setup is the same as described in (d), except BA4 was evaluated
941 rather than BA7. (Right) Quantification of membrane β5 intensities were quantified and
942 normalized to membrane loading control K_v1.2. # indicates samples excluded from analysis on
943 basis of high abnormal actin and K_v1.2 signal. Data (right) are mean ± SEM normalized to ε3/3
944 unaffected. *p<0.05 by Two-Way ANOVA Fisher's LSD test relative to BA4 ε3/3 unaffected.

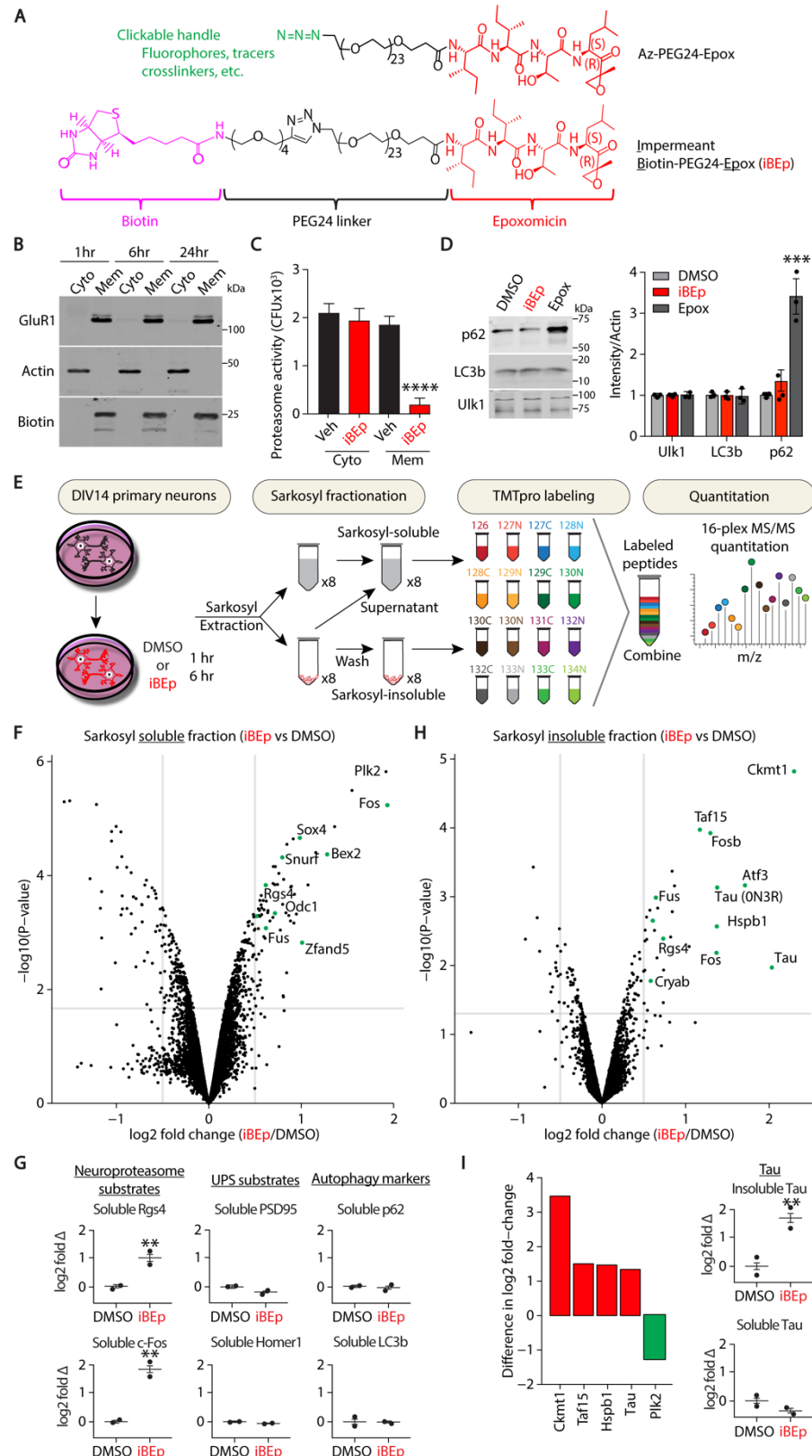


Figure 4
Paradise et al, 2023

946 **Figure 4: Quantitative proteomics reveals that selective inhibition of neuroproteasomes
947 induces accumulation of sarkosyl-insoluble Tau**

948

949 **(A)** (Top) Structure of azide-PEG24-epoxomicin handle to enable rapid conjugation of linkers to
950 global proteasome inhibitor epoxomicin using Click chemistry. (Bottom) Structure of
951 Neuroproteasome-specific inhibitor impermeant Biotin-PEG24-Epoxomicin (iBEp).

952

953 **(B)** Assessing permeability of iBEp in primary neurons. Primary cortical neurons obtained from
954 WT mice were treated with 1 μ M iBEp for 1, 6 and 24 hours and subjected to membrane
955 fractionation. Cytosolic (Cyto) and membrane (Mem) fractions were immunoblotted using
956 indicated antibodies.

957

958 **(C)** Proteasome catalytic activity of membrane (Mem) and cytosolic (Cyto) fractions of neurons
959 treated with iBEp. DIV14 primary cortical neurons obtained from WT mice were treated with
960 DMSO (black) and iBEp (red) for 6 hours and subjected to membrane fractionation. Proteasome
961 catalytic activity was assessed by monitoring degradation of Suc-LLVY-AMC; proteasome-
962 dependent cleavage of the substrate increases AMC fluorescence. N=3 biological replicates.
963 ***p<0.0001 by One-Way ANOVA.

964

965 **(D)** Primary neurons treated with iBEp probed for autophagy markers. DIV14 primary cortical
966 neurons obtained from WT mice were treated with DMSO (light gray), iBEp (red) or
967 Epoxomicin (Epox, dark gray). Lysates were immunoblotted using indicated antibodies against
968 common autophagy markers. Quantification of p62, LC3b, and Ulk1 intensities normalized to
969 Actin. Data (right) are mean \pm SEM normalized to respective DMSO controls. N=4 biological
970 replicates, ***p<0.001 by One-Way ANOVA.

971

972 **(E)** Schematic to analyze changes in sarkosyl-soluble and insoluble proteomes in response to
973 neuroproteasome inhibition. DIV14 primary neurons obtained from WT mice were treated with
974 DMSO or iBEp for 1 and 6 hours and subjected to sarkosyl fractionation. Sarkosyl-soluble and
975 insoluble fractions were labeled with Tandem Mass Tags (TMTpro) for quantitative mass
976 spectrometry.

977

978 **(F)** Differential enrichment of proteins in the sarkosyl-soluble fraction of neurons treated with
979 iBEp versus DMSO was analyzed and plotted as log2-fold change vs $-\log_{10}(P\text{-value})$. Green
980 dots represent proteins enriched in the iBEp treatment compared to DMSO treatment.

981

982 **(G)** Graphs plotting the log2-fold change of select Neuroproteasome substrates enriched in the
983 sarkosyl-soluble fraction from MS analysis in (f) compared to UPS substrates and autophagy
984 markers **p<0.01 (adjusted p-value after multiple corrections).

985

986 **(H)** Differential enrichment of proteins in the sarkosyl-insoluble fraction of neurons treated with
987 iBEp versus DMSO was analyzed and plotted as log2-fold change vs $-\log_{10}(P\text{-value})$. Green
988 dots represent proteins enriched in the iBEp treatment compared to DMSO treatment.
989
990 **(I)** (Left) Identification of proteins which are exclusively enriched in the insoluble fraction with
991 no corresponding change in the soluble fraction (red). Plk2 represents the only protein which is
992 enriched in the soluble fraction with no corresponding change in the insoluble fraction (green).
993 Proteins plotted as differences in log2 fold changes. (Right) Graphs plotting the log2 fold
994 changes of insoluble Tau (top) and soluble Tau (bottom) enriched in neurons treated with iBEp
995 vs DMSO. ** $p < 0.01$ (adjusted p-value after multiple corrections).

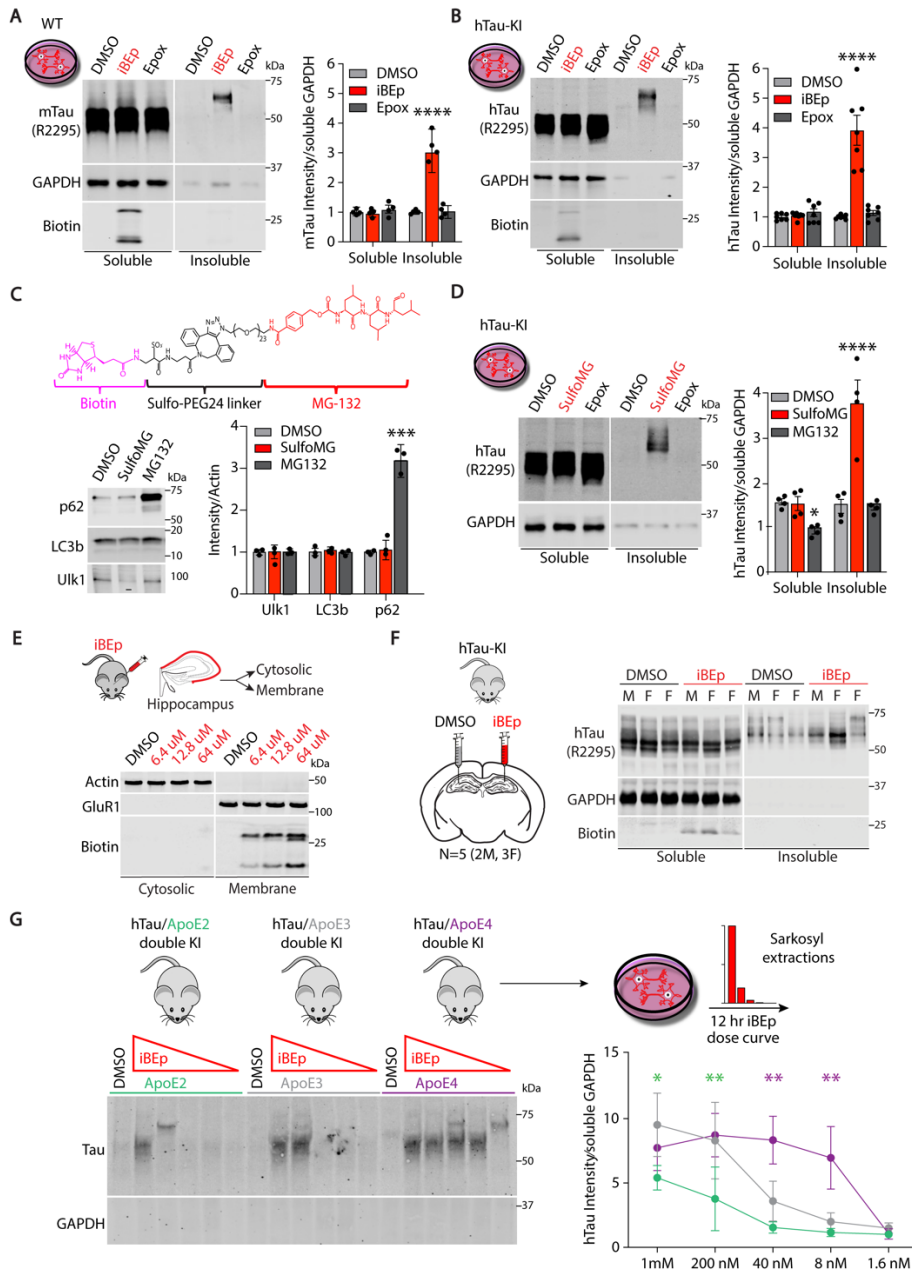


Figure 5
Paradise et al, 2023

996

997 **Figure 5: Neuroproteasomes are differentially regulated by ApoE isoforms to determine**
998 **formation of endogenous sarkosyl-insoluble Tau inclusions**

999

1000 **(A) Effect of neuroproteasome-specific inhibitor iBEP on Tau aggregation in primary neurons.**
1001 DIV14 primary cortical neurons obtained from WT mice were treated with DMSO (light gray),
1002 1μM iBEP (red), or 1 μM Epoxomicin (Epox, dark gray) for 12 hours and were subjected to
1003 sarkosyl fractionation. Sarkosyl-soluble (Soluble) and sarkosyl-insoluble (Insoluble) fractions
1004 were immunoblotted using following antibodies: R2295 for total Tau, GAPDH, and fluorescent

1005 Streptavidin (Biotin). Quantification of soluble and insoluble murine Tau (mTau) intensities
1006 normalized to soluble GAPDH. Data (right) are mean ± SEM normalized to respective DMSO
1007 controls. N=4 biological replicates, ***p<0.0001 by One-Way ANOVA Tukey's Multiple
1008 Comparison Test, sarkosyl-soluble and insoluble analyzed separately.
1009

1010 **(B)** Effect of neuroproteasome inhibition on aggregation of human Tau (hTau). Experiment done
1011 identically as in (a) but using DIV14 primary cortical neurons obtained from hTau-knock-in
1012 (hTau-KI) mice instead of WT mice. Data (right) are mean ± SEM normalized to respective
1013 DMSO controls, N=7 biological replicates, ***p<0.0001 by One-Way ANOVA Tukey's
1014 Multiple Comparison Test.
1015

1016 **(C)** Generation of reversible neuroproteasome inhibitors to test effects of neuroproteasome
1017 inhibition. (Top) Structure of Sulfo-MG132 (SulfoMG). (Bottom) DIV14 hTau-KI primary
1018 cortical neurons were treated with DMSO (light gray), 1µM SulfoMG (red), or 1µM MG132
1019 (dark gray), with or without 10µg/mL cycloheximide (CHX), and immunoblotted using indicated
1020 antibodies. Quantification of p62, LC3b, Ulk1 intensities normalized to Actin. -CHX data (right)
1021 are mean ± SEM normalized to DMSO. N=3 biological replicates, ***p<0.001 by One-Way
1022 ANOVA Tukey's Multiple Comparison Test.
1023

1024 **(D)** Effect of reversible neuroproteasome inhibition using SulfoMG on Tau aggregation. DIV14
1025 primary cortical neurons obtained from hTau-KI mice were treated as described in (e) and
1026 processsd as described in (b). Sarkosyl-soluble (Soluble) and sarkosyl-insoluble (Insoluble)
1027 fractions were immunoblotted using indicated antibodies and fluorescent Streptavidin (Biotin).
1028 Quantification of soluble and insoluble Tau intensities were normalized to soluble GAPDH. Data
1029 (right) are mean ± SEM normalized respective to DMSO controls. N=4 biological replicates,
1030 *p<0.05, ***p<0.0001 by One-Way ANOVA Tukey's Multiple Comparison Test.
1031

1032 **(E)** Testing iBEp permeability *in vivo*. (Top) iBEp or 0.7% DMSO was stereotactically injected
1033 into the CA1 region of the hippocampus in the left hemisphere of WT mice. 72 hours post
1034 injection, hippocampi were isolated and subjected to membrane fractionation without detergent.
1035 (Bottom) Cytosolic and membrane fractions were immunoblotted using indicated antibodies and
1036 fluorescent Streptavidin (Biotin).
1037

1038 **(F)** Effect of neuroproteasome inhibition on Tau aggregation *in vivo*. Four-to-five month old
1039 hTau-KI mice were stereotactically injected with iBEp (red) in the CA1 region of the left
1040 hippocampus and DMSO (gray) was injected contralaterally. The hippocampi were subjected to
1041 sarkosyl fractionation 72 hours post injection. The sarkosyl-soluble (Soluble) and sarkosyl-
1042 insoluble (Insoluble) fractions were immunoblotted using indicated antibodies and fluorescent
1043 streptavidin (Biotin). Quantification of soluble and insoluble Tau intensities normalized to
1044 soluble GAPDH. Data shown (right) are mean ± SEM normalized to DMSO. N= 5 biological

1045 replicates; (2M, 3F), *p<0.05, ***p<0.001 by One-Way ANOVA Tukey's Multiple Comparison
1046 Test.

1047

1048 **(G)** Effect of ApoE isoforms on neuroproteasome-dependent Tau aggregation. DIV14 primary
1049 neurons from hTau/ApoE2 double KI (green), hTau/ApoE3 double KI (gray), and hTau/ApoE4
1050 double KI (purple) mice were incubated with the following iBEp (red) doses: 1000, 200, 40, 8
1051 and 1.6nM. Treated neurons were subjected to sarkosyl extraction and sarkosyl-insoluble
1052 fractions were immunoblotted using indicated antibodies. Quantification of sarkosyl-insoluble
1053 Tau intensity was normalized to soluble GAPDH. Data are mean ± SEM normalized to
1054 respective DMSO controls. N=3 biological replicates, **p<0.01, *p<0.05 by Two-Way
1055 ANOVA Tukey's Multiple Comparisons Test.

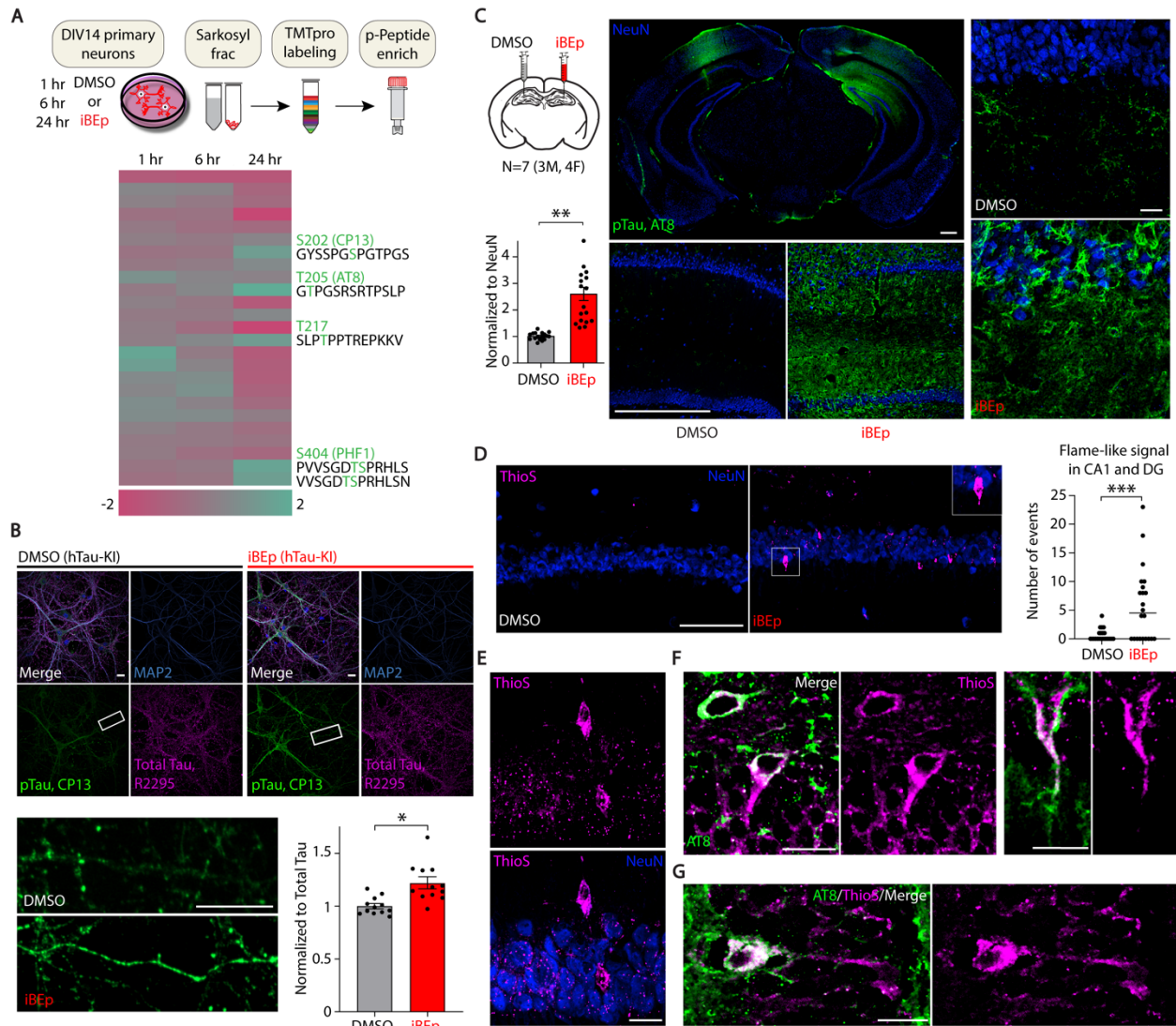


Figure 6
Paradise et al, 2023

1056

1057

1058 **Figure 6: Neuroproteasome inhibition induces endogenous phosphorylated, sarkosyl-
1059 insoluble, Thioflavin S-positive Tau aggregates**

1060

1061 (A) (Top) Schematic of quantitative phosphoproteomics experiments from primary neurons
1062 treated with neuroproteasome inhibitor iBEp. DIV14 primary neurons obtained from WT mice
1063 were treated with 1 μM iBEp for 1, 6, and 24 hours or DMSO and separated into sarkosyl soluble
1064 or insoluble (red) fractions. Samples were processed for quantitative TMTpro-based
1065 phosphoproteomic analysis. (Bottom) Heatmap displays all identified Tau phosphopeptides and
1066 their relative depletion (pink) or enrichment (green) compared to DMSO controls at indicated

1067 timepoints. Select phosphopeptides enriched in iBEp treated neurons over the timecourse are
1068 labeled (green) and antibodies to detect these phosphoepitopes indicated in parenthesis.
1069

1070 **(B)** Immunocytochemical analysis of neurons treated with iBEp to measure Tau phosphorylation.
1071 DIV14 primary hippocampal neurons obtained from hTau-knock-in (hTau-KI) mice treated with
1072 DMSO or iBEp (red) for 12 hours were fixed and stained using indicated antibodies: MAP2
1073 (blue) to label dendrites, phosphorylated Tau (pTau, CP13, green) or total Tau (R2295, purple).
1074 Quantification of pTau signal intensity was normalized to total Tau. Data are mean ± SEM
1075 normalized to DMSO. N=12 (3 biological replicates, 4 images/replicate), *p < 0.05 by Paired T-
1076 test. Scale bars=15μm
1077

1078 **(C)** Immunohistochemical analysis of mice stereotactically injected with iBEp to measure Tau
1079 phosphorylation *in vivo*. Four-to-five month old hTau-KI mice were stereotactically injected
1080 (schematic) with iBEp (red) into the CA1 region of the hippocampus in the left hemisphere and
1081 DMSO (gray) was injected contralaterally (N=7 (3M, 4F)). Mice were collected 72 hours post
1082 injection and sections were stained using indicated antibodies: NeuN (blue) and AT8 (pTau,
1083 green). 4X, 20X and 60X representative images are shown. Quantification of pTau signal
1084 intensity was normalized to NeuN intensity. Analysis was done blinded to experimental
1085 condition. Data are mean ± SEM normalized either to DMSO or iBEP+CHX. n=2
1086 sections/animal, **p<0.01 by Paired T-test/experiment. Scale bars=500μm (left), scale
1087 bar=25μm (right).
1088

1089 **(D)** Immunohistochemical analysis of mice stereotactically injected with iBEp to measure
1090 Thioflavin-S positive Tau aggregates *in vivo*. Four-to-five month old hTau-KI mice were treated
1091 identically to (c), but stained for Thioflavin S (magenta) to visualize β-sheet containing
1092 aggregates and immunostained with NeuN (blue). N=7 (3M, 4F). Left, Vehicle-treated
1093 hippocampus, Right, iBEp-treated hippocampus (red). Inset in iBEp-treated hippocampus
1094 indicates representative example of flame-like Thioflavin-S positive inclusion. Data are
1095 quantification of number of flame-like Thioflavin-S positive inclusions. Counting and analysis
1096 was blinded to experimental condition. ***p<0.001 by one-way ANOVA. Scale bars=100μm.
1097

1098 **(E)** Higher magnification image of flame-like Thioflavin S-positive inclusions (magenta), NeuN
1099 (blue). Top, ThioS alone, Bottom, merge with NeuN. Scale bar=20μm.
1100

1101 **(F, G)** Hippocampal sections from iBEp-injected mice co-stained with Thioflavin S (magenta)
1102 and AT8 (Green), overlap appears white. Images are single Z-plane images to accurately
1103 demonstrate co-localization of ThioS and AT8 staining, demonstrating that some ThioS+
1104 inclusions co-localize with AT8. (F) Contains two representative examples of flame-like ThioS+
1105 inclusions while (G) displays representative example of thread-like inclusions. Scale bar=20μm.

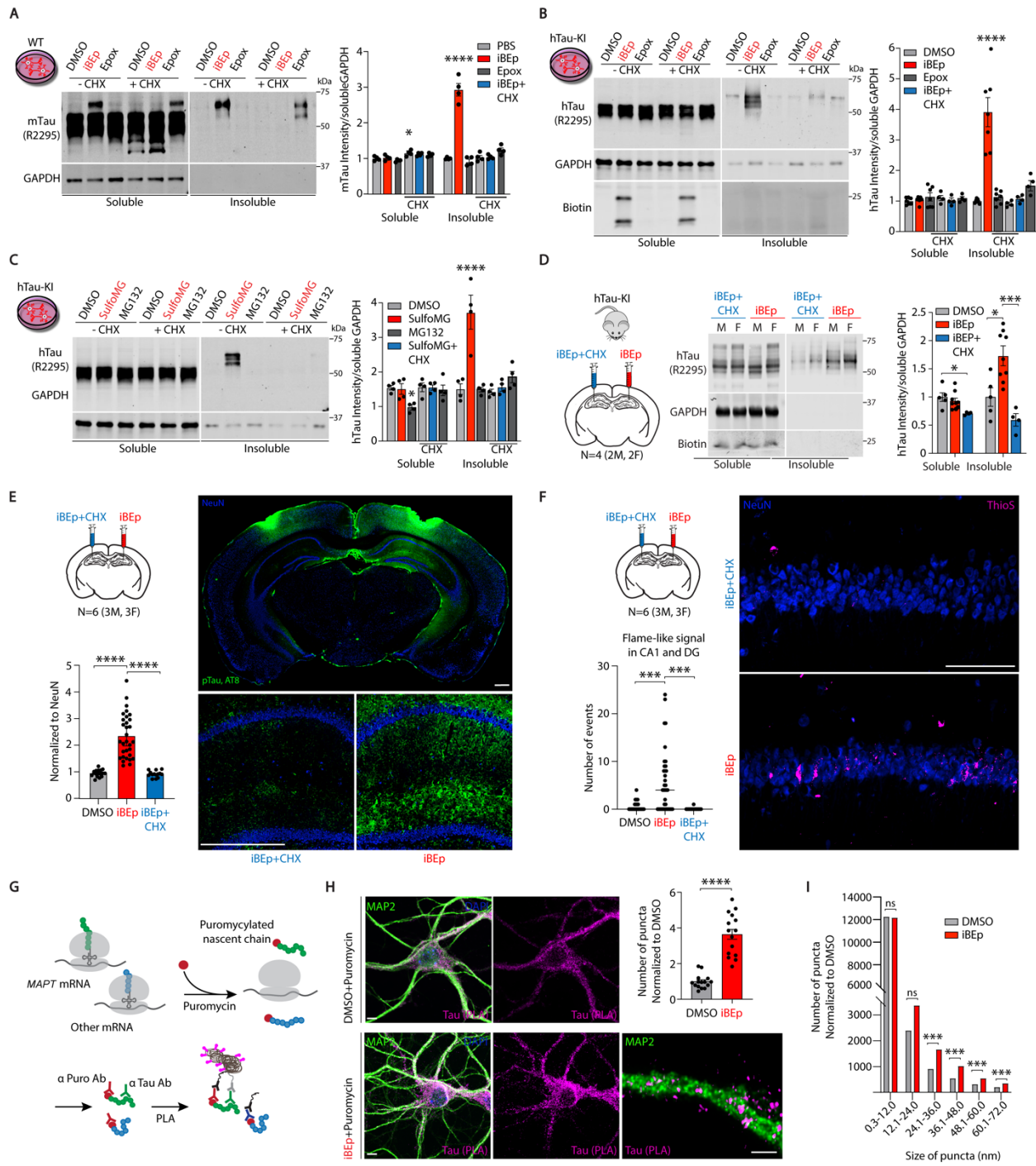


Figure 7
Paradise et al, 2023

1106
1107
1108 **Figure 7. De novo protein synthesis is required for neuroproteasome-dependent induction**
1109 **of endogenous Tau aggregates**
1110

1111 **(A)** Effect of protein synthesis inhibition on neuroproteasome-dependent Tau aggregation.
1112 DIV14 primary cortical neurons obtained from WT mice were treated with DMSO, 1 μ M iBEP,
1113 or 1 μ M Epoxomicin (Epox) for 12 hours, with and without cycloheximide (CHX). Sarkosyl-
1114 soluble (Soluble) and sarkosyl-insoluble (Insoluble) fractions were immunoblotted using
1115 following antibodies: R2295 for total Tau, GAPDH, and fluorescent Streptavidin (Biotin). iBEP
1116 + CHX indicated in blue for emphasis relative to iBEP alone (red). Data (right) are mean \pm SEM
1117 normalized to respective DMSO controls. N=4 biological replicates, ***p<0.001 by One-Way
1118 ANOVA Tukey's Multiple Comparison Test.
1119

1120 **(B)** Effect of protein synthesis inhibition on neuroproteasome-dependent Tau aggregation.
1121 DIV14 primary cortical neurons obtained from hTau-KI mice were treated and processed
1122 identically to (a). iBEP + CHX indicated in blue for emphasis relative to iBEP alone (red). Data
1123 (right) are mean \pm SEM normalized to respective DMSO controls. N=7 biological replicates
1124 without CHX, N=4 with CHX, ***p<0.001 by One-Way ANOVA Tukey's Multiple
1125 Comparison Test.
1126

1127 **(C)** Effect of protein synthesis inhibition on neuroproteasome-dependent Tau aggregation.
1128 DIV14 primary cortical neurons obtained from hTau-KI mice were treated with DMSO, 1 μ M
1129 SulfoMG, or 1 μ M MG132 for 12 hours, with and without cycloheximide (CHX) and processed
1130 identically to (a). SulfoMG + CHX indicated in blue for emphasis relative to SulfoMG alone
1131 (red). Data (right) are mean \pm SEM normalized to respective DMSO controls. N=4 biological
1132 replicates, ***p<0.001 by One-Way ANOVA Tukey's Multiple Comparison Test.
1133

1134 **(D)** Effect of protein synthesis inhibition on neuroproteasome-dependent Tau aggregation *in*
1135 *vivo*. Four-to-five month old hTau-KI mice were stereotactically injected with iBEP in the left
1136 hippocampus and iBEP + CHX were co-injected (blue) contralaterally. Hippocampi were
1137 subjected to sarkosyl fractionation 72 hours post injection. The sarkosyl-soluble (Soluble) and
1138 sarkosyl-insoluble (Insoluble) fractions were immunoblotted using indicated antibodies and
1139 fluorescent streptavidin (Biotin). Quantification of soluble and insoluble Tau intensities
1140 normalized to soluble GAPDH. Data shown (right) are mean \pm SEM normalized to DMSO. N=4
1141 biological replicates (2M, 2F), *p<0.05, ***p<0.001 by One-Way ANOVA Tukey's Multiple
1142 Comparison Test.
1143

1144 **(E)** Four-to-five month old hTau-KI mice were stereotactically injected (schematic) with iBEP
1145 (red) and iBEP + CHX (blue) contralaterally (N=6, (3M, 3F)). Mice were collected 72 hours post
1146 injection and sections were stained using indicated antibodies: NeuN (blue) and AT8 (pTau,
1147 green). 4X, 20X and 60X representative images are shown. Quantification of pTau signal
1148 intensity was normalized to NeuN intensity. Analysis was done blinded to experimental
1149 condition. Data are mean \pm SEM normalized to DMSO. n=3 sections/animal, ***p<0.0001 by
1150 one-way ANOVA. Scale bar=500 μ m

1151
1152 **(F)** Immunohistochemical analysis of hTau-KI mice stereotactically injected (schematic) with
1153 iBEp (red) and iBEp + CHX (blue) contralaterally (N=6, (3M, 3F)). Mice were collected 72
1154 hours post injection and sections and stained with Thioflavin-S and antibodies against NeuN.
1155 Thioflavin S-labeled β -sheet protein structure is stained in magenta, NeuN is stained in blue.
1156 Data are quantification of number of flame-like Thioflavin-S positive inclusions. Counting and
1157 analysis was blinded to experimental condition. ***p<0.001 by one-way ANOVA. Scale
1158 bar=100 μ m (right).
1159
1160 **(G)** Schematic of puro-PLA-Tau experiment. Newly synthesized Tau (green) and other nascent
1161 proteins (blue) labeled with puromycin (red). Coincidence detection between anti-puromycin and
1162 anti-Tau antibodies result in an *in situ* ligation and amplification reaction which can be detected
1163 by fluorescent oligos (pink).
1164
1165 **(H)** Neuroproteasome inhibition induces accumulation of newly synthesized Tau. Primary
1166 DIV14 hippocampal neurons treated with DMSO or iBEp (red) were puromycylated for 10
1167 minutes. Tau-PLA-Puro labeling (pink) denotes newly synthesized Tau puncta, total Map2
1168 positive dendrites (green), DAPI (blue). Higher magnification super-resolution image to bottom
1169 right. Quantification of Tau-PLA-Puro signal intensity was normalized to DMSO. ****p<0.0001
1170 by Paired T-test. Scale bar= 5 μ m.
1171
1172 **(I)** Size distribution of Tau-PLA-Puro puncta. Puncta were binned into varying sizes and then
1173 number of puncta were normalized to the number of puncta seen in each bin with DMSO
1174 treatment. This normalizes for the increase in puncta observed with iBEp treatment, allowing for
1175 a fair comparison in size. ***p<0.001 by Paired T-test/size bin.

1176 **References**

- 1177
- 1178 1. S. Finkbeiner, The Autophagy Lysosomal Pathway and Neurodegeneration. *Cold Spring*
1179 *Harb Perspect Biol* **12**, (2020).
- 1180 2. G. A. Collins, A. L. Goldberg, The Logic of the 26S Proteasome. *Cell* **169**, 792-806
1181 (2017).
- 1182 3. K. V. Ramachandran, S. S. Margolis, A mammalian nervous-system-specific plasma
1183 membrane proteasome complex that modulates neuronal function. *Nat Struct Mol Biol*
1184 **24**, 419-430 (2017).
- 1185 4. K. V. Ramachandran *et al.*, Activity-Dependent Degradation of the Nascentome by the
1186 Neuronal Membrane Proteasome. *Mol Cell* **71**, 169-177 e166 (2018).
- 1187 5. H. Y. He *et al.*, Neuronal membrane proteasomes regulate neuronal circuit activity in
1188 vivo and are required for learning-induced behavioral plasticity. *Proc Natl Acad Sci U S*
1189 *A* **120**, e2216537120 (2023).
- 1190 6. J. Labbadia, R. I. Morimoto, The biology of proteostasis in aging and disease. *Annu Rev*
1191 *Biochem* **84**, 435-464 (2015).
- 1192 7. C. A. Ross, M. A. Poirier, Protein aggregation and neurodegenerative disease. *Nat Med*
1193 **10 Suppl**, S10-17 (2004).
- 1194 8. D. C. Chung, S. Roemer, L. Petrucelli, D. W. Dickson, Cellular and pathological
1195 heterogeneity of primary tauopathies. *Mol Neurodegener* **16**, 57 (2021).
- 1196 9. S. M. K. Glasauer *et al.*, Human tau mutations in cerebral organoids induce a progressive
1197 dyshomeostasis of cholesterol. *Stem Cell Reports* **17**, 2127-2140 (2022).
- 1198 10. Y. Yoshiyama *et al.*, Synapse loss and microglial activation precede tangles in a P301S
1199 tauopathy mouse model. *Neuron* **53**, 337-351 (2007).
- 1200 11. K. Schindowski *et al.*, Alzheimer's disease-like tau neuropathology leads to memory
1201 deficits and loss of functional synapses in a novel mutated tau transgenic mouse without
1202 any motor deficits. *Am J Pathol* **169**, 599-616 (2006).
- 1203 12. D. W. Sanders *et al.*, Distinct tau prion strains propagate in cells and mice and define
1204 different tauopathies. *Neuron* **82**, 1271-1288 (2014).
- 1205 13. M. C. Silva *et al.*, Human iPSC-Derived Neuronal Model of Tau-A152T Frontotemporal
1206 Dementia Reveals Tau-Mediated Mechanisms of Neuronal Vulnerability. *Stem Cell*
1207 *Reports* **7**, 325-340 (2016).
- 1208 14. T. E. Tracy *et al.*, Tau interactome maps synaptic and mitochondrial processes associated
1209 with neurodegeneration. *Cell* **185**, 712-728.e714 (2022).
- 1210 15. I. Grundke-Iqbali, K. Iqbal, Tau pathology generated by overexpression of tau. *Am J*
1211 *Pathol* **155**, 1781-1785 (1999).
- 1212 16. T. F. Gendron, L. Petrucelli, The role of tau in neurodegeneration. *Mol Neurodegener* **4**,
1213 13 (2009).
- 1214 17. S. Dujardin *et al.*, Different tau species lead to heterogeneous tau pathology propagation
1215 and misfolding. *Acta Neuropathol Commun* **6**, 132 (2018).
- 1216 18. D. Xia, J. M. Gutmann, J. Gotz, Mobility and subcellular localization of endogenous,
1217 gene-edited Tau differs from that of over-expressed human wild-type and P301L mutant
1218 Tau. *Sci Rep* **6**, 29074 (2016).
- 1219 19. T. V. Kamath *et al.*, Kinetics of tau aggregation reveals patient-specific tau
1220 characteristics among Alzheimer's cases. *Brain Commun* **3**, fcab096 (2021).

- 1221 20. M. Jouanne, S. Rault, A. S. Voisin-Chiret, Tau protein aggregation in Alzheimer's
1222 disease: An attractive target for the development of novel therapeutic agents. *Eur J Med
1223 Chem* **139**, 153-167 (2017).
- 1224 21. F. Clavaguera *et al.*, Brain homogenates from human tauopathies induce tau inclusions in
1225 mouse brain. *Proc Natl Acad Sci U S A* **110**, 9535-9540 (2013).
- 1226 22. F. Clavaguera *et al.*, Transmission and spreading of tauopathy in transgenic mouse brain.
1227 *Nat Cell Biol* **11**, 909-913 (2009).
- 1228 23. Y. Wang *et al.*, Tau fragmentation, aggregation and clearance: the dual role of lysosomal
1229 processing. *Hum Mol Genet* **18**, 4153-4170 (2009).
- 1230 24. B. Caballero *et al.*, Acetylated tau inhibits chaperone-mediated autophagy and promotes
1231 tau pathology propagation in mice. *Nat Commun* **12**, 2238 (2021).
- 1232 25. J. M. Carosi *et al.*, Retromer regulates the lysosomal clearance of MAPT/tau. *Autophagy*
1233 **17**, 2217-2237 (2021).
- 1234 26. Z. P. Van Acker, M. Bretou, W. Annaert, Endo-lysosomal dysregulations and late-onset
1235 Alzheimer's disease: impact of genetic risk factors. *Mol Neurodegener* **14**, 20 (2019).
- 1236 27. T. Grune *et al.*, Tau protein degradation is catalyzed by the ATP/ubiquitin-independent
1237 20S proteasome under normal cell conditions. *Arch Biochem Biophys* **500**, 181-188
1238 (2010).
- 1239 28. D. C. David *et al.*, Proteasomal degradation of tau protein. *J Neurochem* **83**, 176-185
1240 (2002).
- 1241 29. Y. Wang, E. Mandelkow, Degradation of tau protein by autophagy and proteasomal
1242 pathways. *Biochem Soc Trans* **40**, 644-652 (2012).
- 1243 30. T. Ukmar-Godec *et al.*, Proteasomal degradation of the intrinsically disordered protein
1244 tau at single-residue resolution. *Sci Adv* **6**, eaba3916 (2020).
- 1245 31. U. Kruger, Y. Wang, S. Kumar, E. M. Mandelkow, Autophagic degradation of tau in
1246 primary neurons and its enhancement by trehalose. *Neurobiol Aging* **33**, 2291-2305
1247 (2012).
- 1248 32. Z. Lei, C. Brizzee, G. V. Johnson, BAG3 facilitates the clearance of endogenous tau in
1249 primary neurons. *Neurobiol Aging* **36**, 241-248 (2015).
- 1250 33. S. Feuillette *et al.*, Tau is not normally degraded by the proteasome. *J Neurosci Res* **80**,
1251 400-405 (2005).
- 1252 34. W. Fan *et al.*, NPAS4 Facilitates the Autophagic Clearance of Endogenous Tau in Rat
1253 Cortical Neurons. *J Mol Neurosci* **58**, 401-410 (2016).
- 1254 35. I. Saha *et al.*, The AAA+ chaperone VCP disaggregates Tau fibrils and generates
1255 aggregate seeds. *bioRxiv*, 2022.2002.2018.481043 (2022).
- 1256 36. A. Dincer *et al.*, APOE epsilon4 genotype, amyloid-beta, and sex interact to predict tau in
1257 regions of high APOE mRNA expression. *Sci Transl Med* **14**, eabl7646 (2022).
- 1258 37. Y. Shi *et al.*, ApoE4 markedly exacerbates tau-mediated neurodegeneration in a mouse
1259 model of tauopathy. *Nature* **549**, 523-527 (2017).
- 1260 38. M. S. Baek *et al.*, Effect of APOE epsilon4 genotype on amyloid-beta and tau
1261 accumulation in Alzheimer's disease. *Alzheimers Res Ther* **12**, 140 (2020).
- 1262 39. W. J. Strittmatter *et al.*, Apolipoprotein E: high-avidity binding to beta-amyloid and
1263 increased frequency of type 4 allele in late-onset familial Alzheimer disease. *Proc Natl
1264 Acad Sci U S A* **90**, 1977-1981 (1993).

- 1265 40. D. M. Holtzman, J. Herz, G. Bu, Apolipoprotein E and apolipoprotein E receptors:
1266 normal biology and roles in Alzheimer disease. *Cold Spring Harb Perspect Med* **2**,
1267 a006312 (2012).
- 1268 41. J. M. Castellano *et al.*, Human apoE isoforms differentially regulate brain amyloid- β
1269 peptide clearance. *Sci Transl Med* **3**, 89ra57 (2011).
- 1270 42. M. A. Husain, B. Laurent, M. Plourde, APOE and Alzheimer's Disease: From Lipid
1271 Transport to Physiopathology and Therapeutics. *Front Neurosci* **15**, 630502 (2021).
- 1272 43. J. Miao *et al.*, Pathological Tau From Alzheimer's Brain Induces Site-Specific
1273 Hyperphosphorylation and SDS- and Reducing Agent-Resistant Aggregation of Tau in
1274 vivo. *Front Aging Neurosci* **11**, 34 (2019).
- 1275 44. V. M. Lee, B. J. Balin, L. Otvos, Jr., J. Q. Trojanowski, A68: a major subunit of paired
1276 helical filaments and derivatized forms of normal Tau. *Science* **251**, 675-678 (1991).
- 1277 45. S. Takeda *et al.*, Neuronal uptake and propagation of a rare phosphorylated high-
1278 molecular-weight tau derived from Alzheimer's disease brain. *Nat Commun* **6**, 8490
1279 (2015).
- 1280 46. E. Audouard *et al.*, High-Molecular-Weight Paired Helical Filaments from Alzheimer
1281 Brain Induces Seeding of Wild-Type Mouse Tau into an Argyrophilic 4R Tau Pathology
1282 in Vivo. *Am J Pathol* **186**, 2709-2722 (2016).
- 1283 47. X. Zhan *et al.*, Generation of BAF53b-Cre transgenic mice with pan-neuronal Cre
1284 activities. *Genesis* **53**, 440-448 (2015).
- 1285 48. H. C. Besche, W. Haas, S. P. Gygi, A. L. Goldberg, Isolation of mammalian 26S
1286 proteasomes and p97/VCP complexes using the ubiquitin-like domain from HHR23B
1287 reveals novel proteasome-associated proteins. *Biochemistry* **48**, 2538-2549 (2009).
- 1288 49. T. Sasaki, T. Kikuchi, N. Yumoto, N. Yoshimura, T. Murachi, Comparative specificity
1289 and kinetic studies on porcine calpain I and calpain II with naturally occurring peptides
1290 and synthetic fluorogenic substrates. *J Biol Chem* **259**, 12489-12494 (1984).
- 1291 50. D. T. Lin *et al.*, Regulation of AMPA receptor extrasynaptic insertion by 4.1N,
1292 phosphorylation and palmitoylation. *Nat Neurosci* **12**, 879-887 (2009).
- 1293 51. M. Ascaño, A. Richmond, P. Borden, R. Kuruvilla, Axonal targeting of Trk receptors via
1294 transcytosis regulates sensitivity to neurotrophin responses. *J Neurosci* **29**, 11674-11685
1295 (2009).
- 1296 52. T. V. Huynh *et al.*, Lack of hepatic apoE does not influence early Abeta deposition:
1297 observations from a new APOE knock-in model. *Mol Neurodegener* **14**, 37 (2019).
- 1298 53. H. Fu, J. Hardy, K. E. Duff, Selective vulnerability in neurodegenerative diseases. *Nat
1299 Neurosci* **21**, 1350-1358 (2018).
- 1300 54. M. A. DeTure, D. W. Dickson, The neuropathological diagnosis of Alzheimer's disease.
1301 *Mol Neurodegener* **14**, 32 (2019).
- 1302 55. S. Yan *et al.*, Sex modifies APOE epsilon4 dose effect on brain tau deposition in
1303 cognitively impaired individuals. *Brain* **144**, 3201-3211 (2021).
- 1304 56. S. Yan *et al.*, Association of sex and APOE epsilon4 with brain tau deposition and
1305 atrophy in older adults with Alzheimer's disease. *Theranostics* **10**, 10563-10572 (2020).
- 1306 57. S. Oveisgharan *et al.*, Sex differences in Alzheimer's disease and common
1307 neuropathologies of aging. *Acta Neuropathol* **136**, 887-900 (2018).
- 1308 58. C. M. Mazure, J. Swendsen, Sex differences in Alzheimer's disease and other dementias.
1309 *Lancet Neurol* **15**, 451-452 (2016).

- 1310 59. P. Tiraboschi *et al.*, Impact of APOE genotype on neuropathologic and neurochemical
1311 markers of Alzheimer disease. *Neurology* **62**, 1977-1983 (2004).
- 1312 60. J. M. Prasad, M. Migliorini, R. Galisteo, D. K. Strickland, Generation of a Potent Low
1313 Density Lipoprotein Receptor-related Protein 1 (LRP1) Antagonist by Engineering a
1314 Stable Form of the Receptor-associated Protein (RAP) D3 Domain. *J Biol Chem* **290**,
1315 17262-17268 (2015).
- 1316 61. A. Laatsch *et al.*, Low density lipoprotein receptor-related protein 1 dependent
1317 endosomal trapping and recycling of apolipoprotein E. *PLoS One* **7**, e29385 (2012).
- 1318 62. D. Lee *et al.*, RAP uses a histidine switch to regulate its interaction with LRP in the ER
1319 and Golgi. *Mol Cell* **22**, 423-430 (2006).
- 1320 63. P. May *et al.*, Neuronal LRP1 functionally associates with postsynaptic proteins and is
1321 required for normal motor function in mice. *Mol Cell Biol* **24**, 8872-8883 (2004).
- 1322 64. Q. Liu *et al.*, Neuronal LRP1 knockout in adult mice leads to impaired brain lipid
1323 metabolism and progressive, age-dependent synapse loss and neurodegeneration. *J
1324 Neurosci* **30**, 17068-17078 (2010).
- 1325 65. C. Lane-Donovan, J. Herz, ApoE, ApoE Receptors, and the Synapse in Alzheimer's
1326 Disease. *Trends Endocrinol Metab* **28**, 273-284 (2017).
- 1327 66. R. E. Pitas, J. K. Boyles, S. H. Lee, D. Foss, R. W. Mahley, Astrocytes synthesize
1328 apolipoprotein E and metabolize apolipoprotein E-containing lipoproteins. *Biochim
1329 Biophys Acta* **917**, 148-161 (1987).
- 1330 67. P. B. Verghese *et al.*, ApoE influences amyloid-beta (Abeta) clearance despite minimal
1331 apoE/Abeta association in physiological conditions. *Proc Natl Acad Sci U S A* **110**,
1332 E1807-1816 (2013).
- 1333 68. D. S. Liu *et al.*, APOE4 enhances age-dependent decline in cognitive function by down-
1334 regulating an NMDA receptor pathway in EFAD-Tg mice. *Mol Neurodegener* **10**, 7
1335 (2015).
- 1336 69. E. Nwabuisi-Heath, G. W. Rebeck, M. J. Ladu, C. Yu, ApoE4 delays dendritic spine
1337 formation during neuron development and accelerates loss of mature spines in vitro. *ASN
1338 Neuro* **6**, e00134 (2014).
- 1339 70. M. J. Kim, A. W. Dunah, Y. T. Wang, M. Sheng, Differential roles of NR2A- and NR2B-
1340 containing NMDA receptors in Ras-ERK signaling and AMPA receptor trafficking.
1341 *Neuron* **46**, 745-760 (2005).
- 1342 71. J. G. Hanley, L. Khatri, P. I. Hanson, E. B. Ziff, NSF ATPase and alpha-/beta-SNAPs
1343 disassemble the AMPA receptor-PICK1 complex. *Neuron* **34**, 53-67 (2002).
- 1344 72. P. Manral *et al.*, Can apolipoproteins and complement factors be biomarkers of
1345 Alzheimer's disease? *Curr Alzheimer Res* **9**, 935-943 (2012).
- 1346 73. B. Xu *et al.*, A quantitative proteomic analysis reveals the potential roles of PRDX3 in
1347 neurite outgrowth in N2a-APPswe cells. *Biochem Biophys Res Commun* **604**, 144-150
1348 (2022).
- 1349 74. P. Oeckl *et al.*, Proteomics in cerebrospinal fluid and spinal cord suggests UCHL1,
1350 MAP2 and GPNMB as biomarkers and underpins importance of transcriptional pathways
1351 in amyotrophic lateral sclerosis. *Acta Neuropathol* **139**, 119-134 (2020).
- 1352 75. S. Rayaprolu *et al.*, Systems-based proteomics to resolve the biology of Alzheimer's
1353 disease beyond amyloid and tau. *Neuropsychopharmacology* **46**, 98-115 (2021).
- 1354 76. N. D. Beckmann *et al.*, Multiscale causal networks identify VGF as a key regulator of
1355 Alzheimer's disease. *Nat Commun* **11**, 3942 (2020).

- 1356 77. Z. Yin *et al.*, Detecting Prognosis Risk Biomarkers for Colon Cancer Through Multi-
1357 Omics-Based Prognostic Analysis and Target Regulation Simulation Modeling. *Front*
1358 *Genet* **11**, 524 (2020).
- 1359 78. R. Hesse *et al.*, Comparative profiling of the synaptic proteome from Alzheimer's disease
1360 patients with focus on the APOE genotype. *Acta Neuropathologica Communications* **7**,
1361 214 (2019).
- 1362 79. E. C. B. Johnson *et al.*, Large-scale proteomic analysis of Alzheimer's disease brain and
1363 cerebrospinal fluid reveals early changes in energy metabolism associated with microglia
1364 and astrocyte activation. *Nature Medicine* **26**, 769-780 (2020).
- 1365 80. L. Ping *et al.*, Global quantitative analysis of the human brain proteome and
1366 phosphoproteome in Alzheimer's disease. *Scientific Data* **7**, 315 (2020).
- 1367 81. L. Meng *et al.*, Epoxomicin, a potent and selective proteasome inhibitor, exhibits in vivo
1368 antiinflammatory activity. *Proc Natl Acad Sci U S A* **96**, 10403-10408 (1999).
- 1369 82. N. Sin *et al.*, Total synthesis of the potent proteasome inhibitor epoxomicin: a useful tool
1370 for understanding proteasome biology. *Bioorg Med Chem Lett* **9**, 2283-2288 (1999).
- 1371 83. B. T. Xin *et al.*, Two-Step Bioorthogonal Activity-Based Protein Profiling of Individual
1372 Human Proteasome Catalytic Sites. *Chembiochem* **21**, 248-255 (2020).
- 1373 84. A. F. Kisseelev, W. A. van der Linden, H. S. Overkleeft, Proteasome inhibitors: an
1374 expanding army attacking a unique target. *Chem Biol* **19**, 99-115 (2012).
- 1375 85. C. R. Pye *et al.*, Nonclassical Size Dependence of Permeation Defines Bounds for
1376 Passive Adsorption of Large Drug Molecules. *J Med Chem* **60**, 1665-1672 (2017).
- 1377 86. P. Matsson, J. Kihlberg, How Big Is Too Big for Cell Permeability? *J Med Chem* **60**,
1378 1662-1664 (2017).
- 1379 87. G. P. Soriano, H. S. Overkleeft, B. I. Florea, Two-Step Activity-Based Protein Profiling
1380 with the Proteasome System as Model of Study. *Methods Mol Biol* **1491**, 205-215 (2017).
- 1381 88. N. Li *et al.*, Relative quantification of proteasome activity by activity-based protein
1382 profiling and LC-MS/MS. *Nat Protoc* **8**, 1155-1168 (2013).
- 1383 89. J. C. Misas-Villamil *et al.*, Subunit-selective proteasome activity profiling uncovers
1384 uncoupled proteasome subunit activities during bacterial infections. *Plant J* **90**, 418-430
1385 (2017).
- 1386 90. Q. Ding, V. Cecarini, J. N. Keller, Interplay between protein synthesis and degradation in
1387 the CNS: physiological and pathological implications. *Trends Neurosci* **30**, 31-36 (2007).
- 1388 91. W. X. Ding *et al.*, Linking of autophagy to ubiquitin-proteasome system is important for
1389 the regulation of endoplasmic reticulum stress and cell viability. *Am J Pathol* **171**, 513-
1390 524 (2007).
- 1391 92. B. Tang *et al.*, Proteasome inhibitors activate autophagy involving inhibition of PI3K-
1392 Akt-mTOR pathway as an anti-oxidation defense in human RPE cells. *PLoS One* **9**,
1393 e103364 (2014).
- 1394 93. Z. Sha, H. M. Schnell, K. Ruoff, A. Goldberg, Rapid induction of p62 and GABARAPL1
1395 upon proteasome inhibition promotes survival before autophagy activation. *Journal of*
1396 *Cell Biology* **217**, 1757-1776 (2018).
- 1397 94. M. Colledge *et al.*, Ubiquitination regulates PSD-95 degradation and AMPA receptor
1398 surface expression. *Neuron* **40**, 595-607 (2003).
- 1399 95. J. Gao *et al.*, The E3 ubiquitin ligase IDOL regulates synaptic ApoER2 levels and is
1400 important for plasticity and learning. *eLife* **6**, e29178 (2017).

- 1401 96. A. Y. Hung, C. C. Sung, I. L. Brito, M. Sheng, Degradation of postsynaptic scaffold
1402 GKAP and regulation of dendritic spine morphology by the TRIM3 ubiquitin ligase in rat
1403 hippocampal neurons. *PLoS One* **5**, e9842 (2010).
- 1404 97. S. R. Yoshii, N. Mizushima, Monitoring and Measuring Autophagy. *International*
1405 *Journal of Molecular Sciences* **18**, 1865 (2017).
- 1406 98. Q. Guo *et al.*, Targeted Quantification of Detergent-Insoluble RNA-Binding Proteins in
1407 Human Brain Reveals Stage and Disease Specific Co-aggregation in Alzheimer's
1408 Disease. *Front Mol Neurosci* **14**, 623659 (2021).
- 1409 99. C. M. Hales *et al.*, Changes in the detergent-insoluble brain proteome linked to amyloid
1410 and tau in Alzheimer's Disease progression. *Proteomics* **16**, 3042-3053 (2016).
- 1411 100. B. F. Maziuk *et al.*, RNA binding proteins co-localize with small tau inclusions in
1412 tauopathy. *Acta Neuropathologica Communications* **6**, 71 (2018).
- 1413 101. T. Vanderweyde *et al.*, Interaction of tau with the RNA-Binding Protein TIA1 Regulates
1414 tau Pathophysiology and Toxicity. *Cell Rep* **15**, 1455-1466 (2016).
- 1415 102. E. Drummond *et al.*, Proteomic differences in amyloid plaques in rapidly progressive and
1416 sporadic Alzheimer's disease. *Acta Neuropathol* **133**, 933-954 (2017).
- 1417 103. E. Drummond *et al.*, Phosphorylated tau interactome in the human Alzheimer's disease
1418 brain. *Brain* **143**, 2803-2817 (2020).
- 1419 104. G. Pires, B. Ueberheide, T. Wisniewski, E. Drummond, Use of Affinity Purification-
1420 Mass Spectrometry to Identify Phosphorylated Tau Interactors in Alzheimer's Disease.
1421 *Methods Mol Biol* **2561**, 263-277 (2023).
- 1422 105. T. Saito *et al.*, Humanization of the entire murine Mapt gene provides a murine model of
1423 pathological human tau propagation. *J Biol Chem* **294**, 12754-12765 (2019).
- 1424 106. J. L. Guo *et al.*, Unique pathological tau conformers from Alzheimer's brains transmit tau
1425 pathology in nontransgenic mice. *J Exp Med* **213**, 2635-2654 (2016).
- 1426 107. S. Oddo, L. Billings, J. P. Kesslak, D. H. Cribbs, F. M. LaFerla, Abeta immunotherapy
1427 leads to clearance of early, but not late, hyperphosphorylated tau aggregates via the
1428 proteasome. *Neuron* **43**, 321-332 (2004).
- 1429 108. B. P. Tseng, K. N. Green, J. L. Chan, M. Blurton-Jones, F. M. LaFerla, Abeta inhibits the
1430 proteasome and enhances amyloid and tau accumulation. *Neurobiol Aging* **29**, 1607-1618
1431 (2008).
- 1432 109. J. Z. Wang, Y. Y. Xia, I. Grundke-Iqbali, K. Iqbali, Abnormal hyperphosphorylation of
1433 tau: sites, regulation, and molecular mechanism of neurofibrillary degeneration. *J*
1434 *Alzheimers Dis* **33 Suppl 1**, S123-139 (2013).
- 1435 110. A. D. Alonso *et al.*, Hyperphosphorylation of Tau Associates With Changes in Its
1436 Function Beyond Microtubule Stability. *Front Cell Neurosci* **12**, 338 (2018).
- 1437 111. M. Alpaugh *et al.*, Passive immunotherapy against phosphorylated tau improves features of
1438 Huntington's disease pathology. *Mol Ther* **30**, 1500-1522 (2022).
- 1439 112. L. Cao *et al.*, Pseudo-phosphorylation at AT8 epitopes regulates the tau truncation at
1440 aspartate 421. *Exp Cell Res* **370**, 103-115 (2018).
- 1441 113. R. A. Quintanilla, R. von Bernhardi, J. A. Godoy, N. C. Inestrosa, G. V. Johnson,
1442 Phosphorylated tau potentiates A β -induced mitochondrial damage in mature neurons.
1443 *Neurobiol Dis* **71**, 260-269 (2014).
- 1444 114. X. Wang *et al.*, T217-Phosphorylation Exacerbates Tau Pathologies and Tau-Induced
1445 Cognitive Impairment. *J Alzheimers Dis* **81**, 1403-1418 (2021).

- 1446 115. K. Santacruz *et al.*, Tau suppression in a neurodegenerative mouse model improves
1447 memory function. *Science* **309**, 476-481 (2005).
- 1448 116. J. Lewis *et al.*, Neurofibrillary tangles, amyotrophy and progressive motor disturbance in
1449 mice expressing mutant (P301L) tau protein. *Nat Genet* **25**, 402-405 (2000).
- 1450 117. S. Narasimhan *et al.*, Pathological Tau Strains from Human Brains Recapitulate the
1451 Diversity of Tauopathies in Nontransgenic Mouse Brain. *J Neurosci* **37**, 11406-11423
1452 (2017).
- 1453 118. M. S. Hipp, S. H. Park, F. U. Hartl, Proteostasis impairment in protein-misfolding and -
1454 aggregation diseases. *Trends Cell Biol* **24**, 506-514 (2014).
- 1455 119. A. L. Fink, Protein aggregation: folding aggregates, inclusion bodies and amyloid. *Fold
1456 Des* **3**, R9-23 (1998).
- 1457 120. T. Ishihara *et al.*, Age-dependent induction of congophilic neurofibrillary tau inclusions
1458 in tau transgenic mice. *Am J Pathol* **158**, 555-562 (2001).
- 1459 121. S. tom Dieck *et al.*, Direct visualization of newly synthesized target proteins in situ. *Nat
1460 Methods* **12**, 411-414 (2015).
- 1461 122. C. Li, J. Gotz, Somatodendritic accumulation of Tau in Alzheimer's disease is promoted
1462 by Fyn-mediated local protein translation. *EMBO J* **36**, 3120-3138 (2017).
- 1463 123. G. S. Getz, C. A. Reardon, Apoprotein E and Reverse Cholesterol Transport. *Int J Mol
1464 Sci* **19**, (2018).
- 1465 124. A. Serrano-Pozo, S. Das, B. T. Hyman, APOE and Alzheimer's disease: advances in
1466 genetics, pathophysiology, and therapeutic approaches. *Lancet Neurol* **20**, 68-80 (2021).
- 1467